

THE NATURE OF THE WARM/HOT INTERGALACTIC MEDIUM I. NUMERICAL METHODS, CONVERGENCE, AND OVI ABSORPTION

BRITTON D. SMITH, ERIC J. HALLMAN^{1,2}, J. MICHAEL SHULL

Center for Astrophysics & Space Astronomy, Department of Astrophysical & Planetary Sciences, 389 UCB, University of Colorado, Boulder, CO, 80309

AND

BRIAN W. O'SHEA

Department of Physics & Astronomy, Michigan State University, East Lansing, MI 48824

Draft version October 22, 2018

ABSTRACT

We perform a series of cosmological simulations using *Enzo*, an Eulerian adaptive-mesh refinement, N-body + hydrodynamical code, applied to study the warm/hot intergalactic medium. The WHIM may be an important component of the baryons missing observationally at low redshift. We investigate the dependence of the global star formation rate and mass fraction in various baryonic phases on spatial resolution and methods of incorporating stellar feedback. Although both resolution and feedback significantly affect the total mass in the WHIM, all of our simulations find that the WHIM fraction peaks at $z \sim 0.5$, declining to 35–40% at $z = 0$. We construct samples of synthetic O VI absorption lines from our highest-resolution simulations, using several models of oxygen ionization balance. Models that include both collisional ionization and photoionization provide excellent fits to the observed number density of absorbers per unit redshift over the full range of column densities ($10^{13} \text{ cm}^{-2} \lesssim N_{\text{OVI}} \lesssim 10^{15} \text{ cm}^{-2}$). Models that include only collisional ionization provide better fits for high column density absorbers ($N_{\text{OVI}} \gtrsim 10^{14} \text{ cm}^{-2}$). The distribution of O VI in density and temperature exhibits two populations: one at $T \sim 10^{5.5} \text{ K}$ (collisionally ionized, 55% of total O VI) and one at $T \sim 10^{4.5} \text{ K}$ (photoionized, 37%) with the remainder located in dense gas near galaxies. While not a perfect tracer of hot gas, O VI provides an important tool for a WHIM baryon census.

Subject headings: cosmology: observations — intergalactic medium — quasars: absorption lines

1. INTRODUCTION

It is well established that the fraction of baryons in the universe that are easily observable drops from nearly 100% at high redshift to less than half by the current epoch. Predictions from Big Bang Nucleosynthesis (Olive et al. 2000; Steigman 2007) and measurements of the cosmic microwave background by Komatsu et al. (2010) are in agreement with the cosmic baryon budget measured by observations of the Ly α forest at $z > 4$. Yet baryon surveys at $z = 0$ consistently find that as many as 60% of those baryons are “missing” (Persic & Salucci 1992; Bristow & Phillipps 1994; Fukugita et al. 1998; Fukugita & Peebles 2004). In the low-redshift intergalactic medium (IGM), approximately 30% of the baryons reside in photoionized diffuse Ly α absorbers (the “Lyman-alpha forest”) and $\sim 10\%$ in hot gas traced by O VI absorbers (Danforth & Shull 2008). For reviews of the missing-baryons problem and observational attempts at a solution, see Bregman (2007) and Shull (2003). Early numerical simulations (Cen & Ostriker 1999; Davé et al. 1999, 2001) predicted that a majority of the missing baryons are located in a gaseous phase of moderate to low density and temperatures 10^5 – 10^7 K , known as the warm/hot intergalactic medium (WHIM). These simulations and many that followed showed that many baryons

are heated into the WHIM phase via gravitational shocks from gas falling onto dark-matter filaments and halos, and through galactic outflows and stellar feedback.

WHIM gas is quite tenuous and difficult to observe, with baryon overdensities of typically $\delta_H \equiv \rho_b/\bar{\rho}_b \approx 0.1 - 100$. Here, ρ_b and $\bar{\rho}_b$ are the baryon density and mean baryon density, estimated at $\bar{\rho}_b \equiv \Omega_b \rho_{cr,0} (1+z)^3 = (4.26 \times 10^{-31} \text{ g cm}^{-3})(1+z)^3$, where $\rho_{cr,0}$ is the critical density of the universe at $z = 0$. The method for probing the WHIM that has proved most fruitful thus far is the detection of the O VI doublet ($\lambda\lambda 1032, 1038$) in absorption in the low-redshift Ly α forest, first accomplished by Tripp et al. (2000). In collisional ionization equilibrium (CIE), O VI reaches its peak abundance fraction, $f_{\text{OVI}} \approx 0.2$, at $T \sim 10^{5.45} \text{ K}$ (Sutherland & Dopita 1993), potentially making it an ideal tracer of WHIM gas below 10^6 K . Since the first detections, large surveys of low-redshift O VI absorption lines have been completed (Danforth & Shull 2005, 2008; Danforth et al. 2006; Tripp et al. 2008; Thom & Chen 2008a,b), providing statistical datasets for comparison with simulations. Furlanetto et al. (2005) showed that O VI and O VII absorption statistics can be fit reasonably well by models that assume these systems to be generated in a network of virial and infall shocks that surround cosmological halos. Cen & Fang (2006) were able to broadly reproduce the observed distribution in column density of O VI absorbers, quantified as the number of absorbers per unit redshift (dN/dz), by including a non-equilibrium treatment of oxygen ionization balance

britton.smith@colorado.edu, michael.shull@colorado.edu

¹ National Science Foundation Astronomy and Astrophysics Postdoctoral Fellow

² Institute for Theory and Computation, Harvard-Smithsonian Center for Astrophysics, Cambridge, MA 02138

and stellar feedback from galactic superwinds. However, they did not explicitly study whether these absorbers are tracing the WHIM. More recently, Oppenheimer & Davé (2009) found that a majority of O VI absorption systems in their simulations arise from cold ($T \sim 15,000$ K) gas that is primarily photoionized. They suggested that O VI may not trace the shock-heated WHIM at all. Kang et al. (2005) arrived at a similar conclusion. However, the radiative cooling method of Oppenheimer & Davé (2009) only accounted for the influence of photoionization on the cooling of H and He, but not the metals, whose cooling rate was calculated assuming CIE. At moderately high metallicities ($Z \gtrsim 0.1Z_{\odot}$), this can lead to an overestimate of the total cooling by more than an order of magnitude for $T < 10^5$ K. An excellent demonstration of this is given in Figure 10 of Tepper-Garcia et al. (2010).

In this work, we present the results of a new set of numerical simulations designed to study the nature of the WHIM and its relation to low-redshift metal absorption systems. This paper is the first in a series in which we use the results of these and additional simulations to study the observational signatures of the WHIM. Our primary goals in this first paper are to validate our approach and provide initial predictions. In Section 2, we detail the numerical methods employed in this work. In Section 3, we discuss the initial results of these simulations. To understand the extent to which these simulations can be trusted, we begin by examining how well they are converged, a topic that has received little previous attention. We use our highest-resolution simulations to create samples of synthetic O VI absorption lines for comparison with observations. We then take a closer look at the physical environment associated with the O VI in our simulations, in order to gauge its usefulness as a WHIM tracer. We conclude with a discussion and summary in Section 4.

2. METHODS

In order to understand the dependence of WHIM characteristics on the properties of the simulations, we carry out a large number of cosmological simulations with varying spatial resolution, box size, and physical parameters. In every simulation, the number of grid cells is equal to the number of dark-matter particles. All of the simulations are initialized at $z = 99$ in a Λ CDM universe with a power spectrum of density fluctuations given by Eisenstein & Hu (1999). The cosmological parameters are $(\Omega_b, \Omega_{\text{CDM}}, \Omega_{\Lambda}, h, \sigma_8, n) = (0.0441, 0.2239, 0.732, 0.704, 0.82, 1)$, in reasonable agreement with the WMAP-7 findings (Komatsu et al. 2010). All simulations with the same box size are initialized using identical random seeds, and thus have the same large-scale structure, allowing us to isolate the effects of resolution. Simulations with different box sizes have different random seeds. A summary of the simulations and their distinguishing features is given in Table 1. We now describe the setup and methodology in further detail.

2.1. The Enzo Code

We performed the entire suite of simulations with the Eulerian adaptive mesh-refinement (AMR), hydrodynamics + N-body code, **Enzo**³ (Bryan & Norman 1997;

O’Shea et al. 2005a,b). The equations of hydrodynamics are solved using the ZEUS hydrodynamic solver of Stone & Norman (1992). The evolution of collisionless dark matter is computed with an N-body solver that uses a particle-mesh (PM) gravity solver (Efstathiou et al. 1985; Hockney & Eastwood 1988). The AMR functionality of **Enzo** provides the capability to dynamically add resolution to regions of the computational domain where it may be required for a variety of reasons, such as baryonic or dark-matter overdensity, resolving the Jeans length or shocks. This makes it possible to have high resolution in regions of interest while ignoring less important areas, thus limiting computational costs. However, since the WHIM is thought to reside in regions of relatively low overdensity ($0.1 \lesssim \delta_H \equiv \rho_b/\bar{\rho}_b \lesssim 100$), a very large fraction of the computational domain must be properly resolved. Rather than allowing for vast regions of adaptive refinement throughout the domain, which can introduce significant computational cost simply to manage to the hierarchy of grid patches, we instead choose to run with AMR disabled and to perform simulations with large, static grids, referred to here as “unigrid” simulations.

2.2. Star Formation and Feedback

Star formation is a process that occurs on physical scales many orders of magnitude below the resolution limit of cosmological simulations, yet the products (radiation, thermal energy, and heavy elements) have significant influence on the evolution of structure on large scales. Numerical simulations must employ models based on our limited understanding of the physical conditions that produce stars and the impact they have on their surroundings, on the physical scales relevant to the simulations. Numerous prescriptions for feedback have been introduced with slightly varying parameterizations, (e.g., Cen & Ostriker (1992); Springel & Hernquist (2003a); Schaye & Dalla Vecchia (2008)), that are capable of broadly reproducing the observed star formation history (Hopkins & Beacom 2006).

We use a modified version of the prescription of Cen & Ostriker (1992) in our simulations, which we describe briefly here. Any grid cell is capable of forming stars if the following criteria are met: baryon overdensity, defined here and only here as $\rho_b/(\rho_{c,0}(1+z)^3) > 100$, where $\rho_{c,0}$ is the critical density at $z = 0$; the velocity divergence is negative; and the cooling time is less than the dynamical time. In all other places, we define baryon overdensity as $\rho_b/\bar{\rho}_b$. The original prescription of Cen & Ostriker (1992) calls for the additional check of Jeans instability. However, we find that in large-scale, fixed-grid simulations, this final criterion is always met, following satisfaction of the first three requirements. Therefore, we ignore the check for Jeans instability as a cost-saving measure. If all three listed criteria are satisfied, then a “star particle,” representing a large collection of stars, is formed within the grid cell with a total mass,

$$m_* = f_* m_{\text{cell}} \frac{\Delta t}{t_{\text{dyn}}}, \quad (1)$$

where f_* is an efficiency parameter, m_{cell} is the baryon mass in the cell, t_{dyn} is the dynamical time of the combined baryon and dark matter fluid, and Δt is the hydrodynamical timestep. Subsequently, this much gas mass

³ <http://code.google.com/p/enzo>

Table 1
Parameters of Simulations

Run	l (Mpc/h)	$N_{\text{cells}}^{1/3}$	Δx (kpc/h)	m_{dm} (M_{\odot}/h)	Feedback Method	Metal Yield (y)
25_256_0	25	256	98	6×10^7	0	-
25_384_0	25	384	65	2×10^7	0	-
25_512_0	25	512	49	7×10^6	0	-
25_768_0	25	768	33	2×10^6	0	-
25_1024_0	25	1024	24	9×10^5	0	-
25_256_1	25	256	98	5×10^7	1	0.025
25_384_1	25	384	65	2×10^7	1	0.025
25_512_1	25	512	49	7×10^6	1	0.025
25_768_1	25	768	33	2×10^6	1	0.025
25_768_1b	25	768	33	2×10^6	1	0.005
25_256_2	25	256	98	6×10^7	2	0.025
25_384_2	25	384	65	2×10^7	2	0.025
25_512_2	25	512	49	7×10^6	2	0.025
25_768_2	25	768	33	2×10^6	2	0.025
50_512_0	50	512	98	6×10^7	0	-
50_768_0	50	768	65	2×10^7	0	-
50_1024_0	50	1024	49	7×10^6	0	-
50_512_1	50	512	98	6×10^7	1	0.025
50_768_1	50	768	65	2×10^7	1	0.025
50_768_1b	50	768	65	2×10^7	1	0.005
50_1024_1	50	1024	49	7×10^6	1	0.025
50_512_2	50	512	98	6×10^7	2	0.025
50_768_2	50	768	65	2×10^7	2	0.025
50_768_2b	50	768	65	2×10^7	2	0.005
50_1024_2	50	1024	49	7×10^6	2	0.025

Note. — Run: simulation name, given as (l)-($N_{\text{cells}}^{1/3}$)-(feedback method), where l is the comoving box size and $N_{\text{cells}}^{1/3}$ is the number of grid cells along each edge of the box. The total number of grid cells is equal to the number of dark matter particles. Δx : comoving grid-cell size. m_{dm} : dark matter particle mass. Feedback method: 0: adiabatic (no radiative cooling, feedback from star formation, or ionizing UV background); 1: local method; 2: distributed method. Metal yield: fraction of stellar mass returned to gas as metals (m_{metals}/m_*).

is also removed from the grid cell as the star particle is formed, ensuring mass conservation.

While the star particle is formed instantaneously within the simulation, feedback is assumed to occur over a longer time scale, which more accurately reflects the gradual process of star formation. In a single timestep of the simulation, the amount of mass from a star particle converted into newly formed stars is given by

$$\Delta m_{\text{sf}} = m_* \frac{\Delta t}{t_{\text{dyn}}} \frac{(t - t_*)}{t_{\text{dyn}}} e^{-(t-t_*)/t_{\text{dyn}}}, \quad (2)$$

where t is the current time and t_* the formation time of the star particle. Stellar feedback is represented by the injection of thermal energy and the return of gas and metals to the grid, all in amounts proportional to Δm_{sf} . The thermal energy, e , and metal mass, m_{metals} , returned to the grid are given by

$$e = \Delta m_{\text{sf}} c^2 \epsilon, \quad m_{\text{metals}} = \Delta m_{\text{sf}} y, \quad (3)$$

where c is the speed of light, ϵ is the ratio of thermal energy output to total rest-mass energy of the star particle, and y is the fraction of stellar mass returned to the grid as metals. As per Equation 2, the rate of star formation, and hence the rate at which thermal energy and metals are injected into the grid by the star particle, rises linearly, peaking after one dynamical time, then de-

cays exponentially after that. For a given star particle, 30%, 60%, and 90% of the total feedback production has occurred by 1, 2, and 4 dynamical times, respectively. For a threshold baryon overdensity (as defined above) of 100, corresponding roughly to a total overdensity of 600 (assuming the cosmic ratio of baryonic to dark matter), $t_{\text{dyn}} \simeq 1.25 (1+z)^{-3/2}$ Gyr.

We choose parameters for the prescriptions of star formation and feedback similar to those adopted by Cen & Ostriker (1992). We assume a star-formation efficiency, $f_* = 0.1$, a 25% fraction of stellar mass returned to the grid as gas, and $\epsilon = 10^{-5}$. Of the gas returned to the grid, 10% is returned in the form of metals, for a total metal yield, $y = 0.025$, consistent with the calculations of Madau et al. (1996). This metal yield, $y = 1/40$, is consistent with average values in the Milky Way, with a mean star-formation rate (SFR) of $\sim 3 M_{\odot} \text{ yr}^{-1}$, a core-collapse supernova rate of 1 SN every 40 years (from pulsar counts), and an IMF-averaged metal yield of $\sim 3 M_{\odot}$ per supernova. For a Salpeter IMF, the ratio of supernova energy to metal ejecta rest-mass energy is ~ 0.0015 (Bookbinder et al. 1980). With our choice of y and ϵ , this implies that approximately 27% of the total supernova energy is converted into feedback energy. As one of the main goals of this work is to understand the relation between metals and the WHIM, we have also run three

additional simulations with the metal yield decreased by a factor of 5 to $y = 0.005$. Schaye et al. (2010) investigated the dependence of the global star formation history on the various star formation and feedback parameters, finding it difficult to induce a significant deviation. A parameter study performed as a part of this project showed the star formation history to be robust to changes in the prescription parameters. This effect is primarily due to the fact that star formation is limited by the amount of cold, collapsing gas, which is independent of the choice of parameter values.

In this paper, we investigate two different methods for injecting feedback into the grid: (1) depositing all of the feedback into the grid cell where the star particle exists; and (2) distributing an equal amount among the central cell and its 26 nearest neighbors. Since this entire procedure is designed to account for processes unresolvable by the simulation, neither method should be considered to be representative of the actual physical processes that are occurring, but are, rather, an attempt to mimic the end state of those processes at the multi-kpc scale. Injecting feedback into a single cell has well-known practical limitations: in particular, the great increase in temperature produced by the injection of kinetic or thermal energy in a grid cell with reasonably high density can lead to cooling times that are much shorter than the hydrodynamical timestep, and thus, over-cooling. This diminishes the ability of the stellar products to propagate away from the source. This issue can be mitigated by making the assumption that feedback is able to spread to neighboring grid cells before energy is lost through radiative cooling. This technique was employed by Cen & Fang (2006) to mimic the effect of galactic superwinds. In this work, we distribute feedback to the neighboring cells in the form of thermal energy, gas, and metals, and we do not find it necessary to add kinetic energy. Hereafter, we refer to the method of injecting stellar feedback into the central cell and its 26 neighbors as the *distributed* method, and the method of inserting feedback solely into the central cell as the *local* method.

2.3. Radiative Heating and Cooling

Of utmost importance to properly modeling the evolution of the WHIM is an accurate determination of the thermal state of the baryons within the simulation. Wiersma et al. (2009) showed that including both the radiative cooling from metals and the photoelectric heating from the UV metagalactic background (Haardt & Madau 2001) is vital for simulations of large-scale structure. Unfortunately, a direct calculation of the heating and cooling rates, including metals, requires solving a network of rate equations that is far too large to be viable for millions, and now billions, of grid cells.

We use an efficient computational method, originated by Smith et al. (2008) and similar to Shen et al. (2010), of coupling a multidimensional table of heating and cooling values, precomputed with the photoionization software, `Cloudy`⁴ (Ferland et al. 1998), to a non-equilibrium, primordial chemistry network (Abel et al. 1997; Anniinos et al. 1997). The primordial chemistry network solves for the evolution of six species (H, H⁺, He, He⁺, He⁺⁺, and e⁻), including collisional ionization and

photo-excitation/ionization rates, using a backward differencing formula. We use `Cloudy` version 07.02.01 to construct a grid of heating and cooling rates that vary with density, metallicity, electron fraction, redshift, and temperature. The redshift determines the nature of the UV metagalactic background, given by Haardt & Madau (2001). We construct an analogous grid of values run with H and He and subtract this from the larger grid, so that only the metal heating and cooling rates remain. The rates are normalized by the H number density times the electron number density ($n_{\text{H}} \times n_{\text{e}}$). During the simulation, we use the electron density from the primordial network plus a small, metallicity-dependent correction to calculate the heating and cooling contributions of the metals. We turn on the ionizing (UV) background at $z = 7$. The primordial chemistry network follows the photoionization of H and He, and we interpolate from the grid of data made with `Cloudy` to include both the heating and cooling due to the metals. For $z > 7$, we use a similar grid of heating and cooling data, created with no radiation background, assuming collisional ionization only. The metal heating and cooling terms are included within a coupled chemistry and cooling solver. In order to maintain accuracy, the solver subcycles the cooling and chemistry routines together on timesteps that are no larger than 10% of formation/destruction timescales ($\rho_i/\dot{\rho}_i$) of e⁻ and H, 10% of the cooling time (e/\dot{e} , where e and \dot{e} are the internal energy and its time derivative), and half of the hydrodynamic timestep. Coupling of the chemistry and cooling solver is particularly crucial in regions of high density and metallicity, where the cooling time is very short and the gas can transition from ionized to neutral within a single hydrodynamic timestep.

3. RESULTS

3.1. The Star Formation History

3.1.1. The Effects of Radiative Cooling

We first attempt to quantify the effect of the radiative cooling method chosen by comparing it with a set of four simulations run with less complete treatments. Each of these test simulations has a 25 Mpc/ h box with 512³ grid cells and dark matter particles, with stellar feedback injected into only one cell. These simulations are compared to run 25_512_1. In Figure 1, we plot the comoving star formation rate density for run 25_512_1 and all of the test simulations, along with the compilation of observational data on comoving SFR density by Hopkins & Beacom (2006). The results of this experiment can be summarized very simply: a higher cooling rate results in a higher SFR. The removal of radiative cooling from metals results in a significant decrease in the SFR from $z \sim 5$ to the present. In the absence of both metal cooling and the radiation background (purple line in Figure 1), the peak in the star formation rate is lower by a factor of a few than the control run, and occurs slightly earlier (just before $z = 2$, as opposed to just after.) The low-redshift slope is also much steeper, resulting in a SFR at $z = 0$ that is lower by an order of magnitude. Schaye et al. (2010) observe a similar reduction in the peak SFR, but they do not see the steepening of the slope at low redshift reported here.

The UV background provides additional heating to the gas, making it more difficult to form stars. With only pri-

⁴ <http://nublado.org>

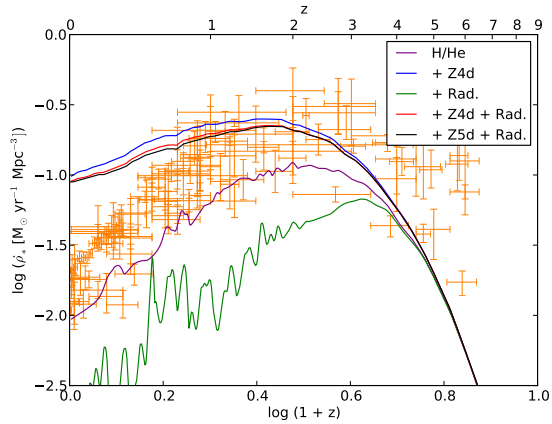


Figure 1. Effect of radiative cooling and radiation background on the comoving star formation rate density plotted over the observational data compiled by Hopkins & Beacom (2006). Shown in black is run 25_512_1, with the full cooling model (non-equilibrium H/He cooling plus a radiation background and metal cooling that includes the effect of the radiation background). Also shown are four additional test simulations with 25 Mpc/h box size and 512^3 grid cells with less complete cooling methods. Purple: only the cooling from atomic H/He with no radiation background; blue: cooling from H/He with no radiation background and metal cooling that does not include the effects of the radiation background; green: cooling from H/He only plus a radiation background; red: cooling from H, He plus radiation background and metal cooling that does not account for the radiation background.

mordial cooling, the addition of the ionizing background has a far greater influence on the ability of the gas to form stars than when metals are included. In the simulation with the radiation background but no metal cooling (green line in Figure 1), the SFR is more than half an order of magnitude lower than the simulation with no radiation background and no metal cooling, or over one and a half orders of magnitude below the control run, which has both a radiation background and metal cooling. When metal cooling is included, the presence of the radiation background makes much less of a difference, as can be seen with the blue and black lines in Figure 1. Photoionization is more effective at reducing the cooling efficiency of primordial gas because of the relative ease with which H and He (compared with heavier elements) are fully ionized, thus eliminating the ability to cool via line emission. Because primordial coolants alone are reduced more efficiently by the presence of the radiation background, it is much more difficult for the gas in these simulations to continue to cool and form stars. Finally, if the metal cooling method does not account for the influence of the radiation background, as was neglected in Oppenheimer & Davé (2009), the potential exists for a significant overestimate in the total cooling. This may have been the primary reason that the above work reported the existence of much colder O VI absorbers than had previously been claimed or is seen in this work. The red line in Figure 1 represents a simulation in which the metal cooling rates do not reflect the presence of the radiation background. Interestingly, we do not see such a dramatic influence on the SFR, as is evidenced by the nearly identical red and black lines in Figure 1.

Not all simulations treat the radiative cooling rate consistently with the ionizing background and metal transport. Because the peak of the radiative cooling rate, at temperatures $4.5 \lesssim \log T \lesssim 6.0$, arises primarily from

electron-impact excitation of bound states of abundant metal ions (C III, C IV, O VI, Ne VIII), a strong UV radiation field will photoionize away those coolants and decrease the cooling. As can be seen in Figure 1, our most complete cooling model over-predicts the SFR at $z < 2$ in this series of simulations, owing to the inability of the feedback prescription to drive the metals away from their source (Springel & Hernquist 2003a). As discussed below, we are able to bring the predicted SFR into better agreement with observations simply by distributing the thermal energy and metals over multiple grid cells.

3.1.2. Convergence

Schaye et al. (2010) note the difficulty of matching the observed SFR at both low and high redshift within a single simulation. At high redshift, extreme resolution is required to resolve the low-mass halos that dominate the global SFR. At low redshift, a large box size is needed to capture the most massive objects forming from large-scale perturbations in the primordial density field that are only recently becoming nonlinear. In Figure 2, we plot the SFR versus redshift and the corresponding stellar density evolution for all simulations listed in Table 1 with metal yield, $y = 0.025$. We do not see convergence in the SFR at high redshift, as noted in previous studies (Springel & Hernquist 2003b; Schaye et al. 2010). Increasing the spatial and gas/dark matter mass resolution, which do not vary independently in our simulations, allows more low-mass halos to be resolved at progressively higher redshifts, continually increasing the SFR. Convergence at $z = 0$ is achieved in our lowest-resolution simulation when using the local feedback method. When using the distributed method, convergence at $z = 0$ is achieved in our second-lowest-resolution simulation. As the resolution is increased, the redshift at which the SFR is converged also increases, as was noted in Springel & Hernquist (2003b). With the local feedback method, the SFR of the two highest resolution runs (25_512_1 vs. 25_768_1 and 50_768_1 vs. 50_1024_1) agree to within 10% for $z \lesssim 1.5$. For the distributed-feedback simulations, this occurs slightly later, at $z \lesssim 1.25$. Since the interval from $z = 1 \rightarrow 0$ represents a majority of the age of the universe, the resulting stellar densities at $z = 0$ are reasonably converged for all but the most poorly resolved simulations.

3.1.3. Feedback and Box Size

All simulations that employ the local feedback method overpredict the SFR at low redshift. This is due to the over-cooling that occurs when feedback is injected only into the central cell, unphysically driving up the gas temperature and the cooling rate (Katz et al. 1996; Balogh et al. 2001). The local feedback simulations with equal resolution have nearly identical SFRs at high redshift. However, those with the larger box size show slightly lower peak rates and a steeper decline at low redshift. This is likely due to the ability of the large-box simulations to form structures with higher virial temperatures, in which much of the gas becomes too hot to form stars. The simulations that use the distributed method display the best agreement with observations. In comparison to their local feedback counterparts, the

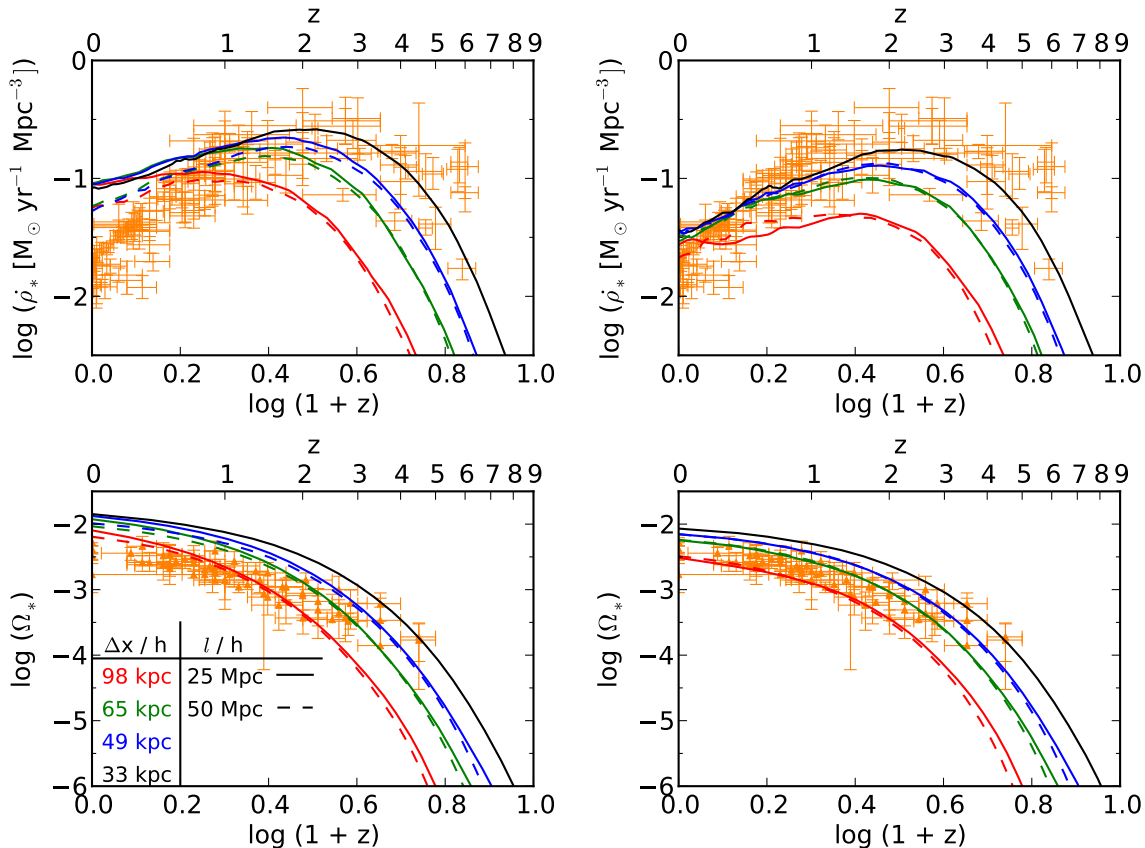


Figure 2. Top panels: comoving star formation rate (SFR) density versus redshift for simulations with varying resolution and box size plotted over the observational data compiled by Hopkins & Beacom (2006). Simulations with the same resolution are shown with the same color: red, $\Delta x = 98 \text{ kpc}/h$; green, $64 \text{ kpc}/h$; blue, $49 \text{ kpc}/h$; and black, $33 \text{ kpc}/h$. Note that spatial and mass resolution are not varied independently in our simulations (see Table 1). Simulations with $25 \text{ Mpc}/h$ box sizes are shown with solid lines, and those with $50 \text{ Mpc}/h$ box sizes are shown with dashed lines. Bottom panels: stellar density in relation to critical density corresponding to top panels plotted over the observational compilation of Wilkins et al. (2008). Left panels denote simulations with local feedback, while right panels denote those with distributed feedback.

distributed-feedback simulations have peak SFRs lower by 35–40%.

The slope of the SFR with redshift (at $z < 2$) is also noticeably steeper in the distributed feedback runs. However, unlike the local feedback simulations, there are no discernable differences between the small-box and large-box simulations of equal resolution when using the distributed method. Comparing the highest resolution simulations of each feedback method, we find the use of local method results in the formation of approximately 1.7 times more stars than the distributed method. In comparison with observational measurements by Wilkins et al. (2008) of the stellar mass density, our simulations still appear to produce too many stars by a factor of a few. However, Wilkins et al. (2008) point out that independent observations of the SFR and the stellar mass density are not consistent with each other; the observed SFR implies a stellar density 2–3 times higher than what is seen. The final conclusion is that spreading stellar feedback over 27 cells, rather than just 1, is largely able to overcome the classic over-cooling problem, yielding a much better fit to fit to observations.

3.2. The Halo Mass Function

In Figure 3, we plot the cumulative halo mass function for all the simulations with distributed feedback and

normal metal yield. To locate halos within our simulations, we use a version of the HOP halo-finding algorithm (Eisenstein & Hut 1998), parallelized by Skory et al. (2010). We show only the mass functions for simulations with distributed feedback. For the range of halos captured in our simulations, there are no notable differences for varying baryonic physics. In comparison with the analytical fit of Warren et al. (2006), we find our simulations to provide a good match for halos with approximately 400 particles or more, regardless of particle mass. This result is in good agreement with numerous, prior *Enzo* simulations, e.g., O’Shea et al. (2005b); Trenti et al. (2010); Skillman et al. (2010).

3.3. The Evolution of Baryon Phases

3.3.1. Convergence

In Figures 4 and 5, we plot the evolution of the baryon fraction in various IGM phases as a function of redshift for the majority of our simulations. We group the plots in rows and columns, showing box size and feedback parameter so as to focus on convergence. We divide the baryons into four phases: *warm* ($T \leq 10^5 \text{ K}$, $\rho_b/\bar{\rho}_b < 1000$); *WHIM* ($10^5 \text{ K} < T \leq 10^7 \text{ K}$, $\rho_b/\bar{\rho}_b < 1000$); *hot* ($T > 10^7 \text{ K}$, $\rho_b/\bar{\rho}_b < 1000$); and *condensed* ($\rho_b/\bar{\rho}_b \geq 1000$). We also include the total mass in stars in the condensed phase. In practice, the gas in the condensed

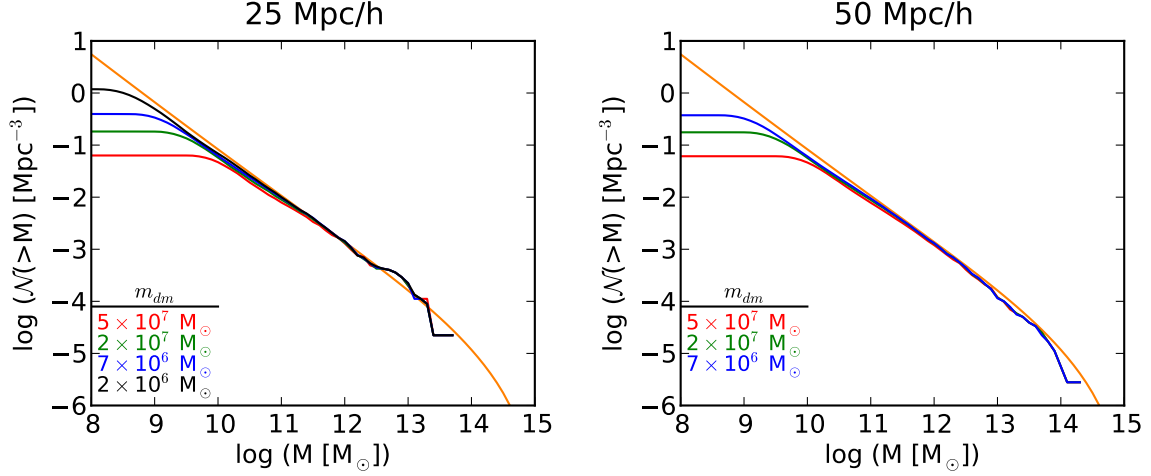


Figure 3. The cumulative halo mass function for all of the simulations with distributed feedback and normal metal yield. Simulations with 25 Mpc/h boxes are shown in the left panel while simulations with 50 Mpc/h boxes are shown in the right panel. Plotted in orange is the analytical fit of Warren et al. (2006). The colors shown here, which indicate the dark matter particle mass within the simulation, are consistent with Figure 2.

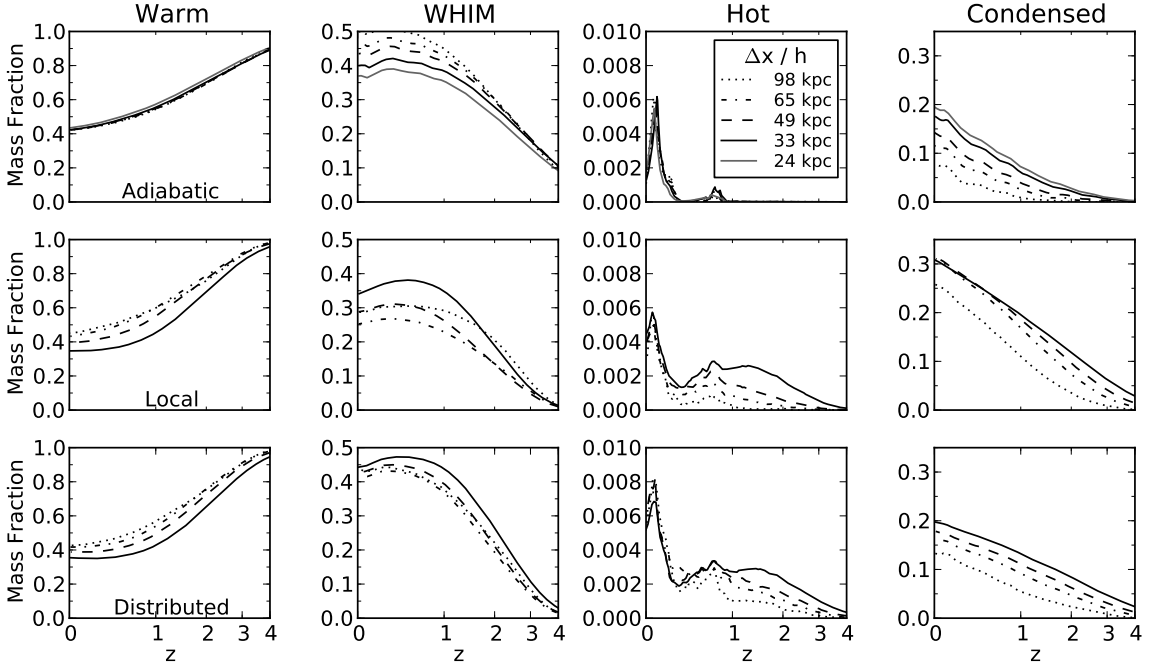


Figure 4. Evolution of baryon mass fraction in the warm ($T < 10^5$ K), WHIM ($10^5 \text{ K} \leq T < 10^7$ K), hot ($T \geq 10^7$ K), and condensed ($\rho_b/\bar{\rho}_b \geq 1000$) phases for the 25 Mpc/h box simulations. The condensed phase includes both gas with baryon overdensity $\delta_H > 1000$ and the total mass in stars. For the warm, WHIM, and hot phases, only gas with $\delta_H < 1000$ is included, such that the total is unity. The top row shows the adiabatic simulations, the middle row shows the simulations with local feedback, and the bottom row shows the simulations with distributed feedback.

phase is almost entirely warm. If we define gas with $\rho_b/\bar{\rho}_b < 1000$ as *diffuse*, we see that the ratio of diffuse to condensed WHIM gas is generally around 20:1 at $z = 0$. The masses of diffuse and condensed hot gas are within a factor of a few of each other, but neither contributes significantly to the total baryon budget within our simulations, mainly due to the somewhat small box sizes. Note that these phase cuts are slightly different from those of other work, such as Davé et al. (2001) and Cen & Ostriker (2006). However, the results are insensitive to these minor differences in definition. We have also measured the evolution of the baryon fractions, with the

overdensity threshold dividing the condensed phase from the other three phases set to 200, and find the variations to be marginal.

In Figure 4, we focus on the simulations with the 25 Mpc/h box size. The top row of Figure 4, which shows the evolution of the adiabatic simulations, reaffirms the idea that shock heating from structure formation plays the primary role in the evolution of the WHIM (Davé et al. 1999, 2001; Cen & Ostriker 1999). Without radiative cooling, star formation, and the UV background, the general trends are similar. Warm, photoionized gas makes up roughly 90% of the total baryon mass at $z = 4$,

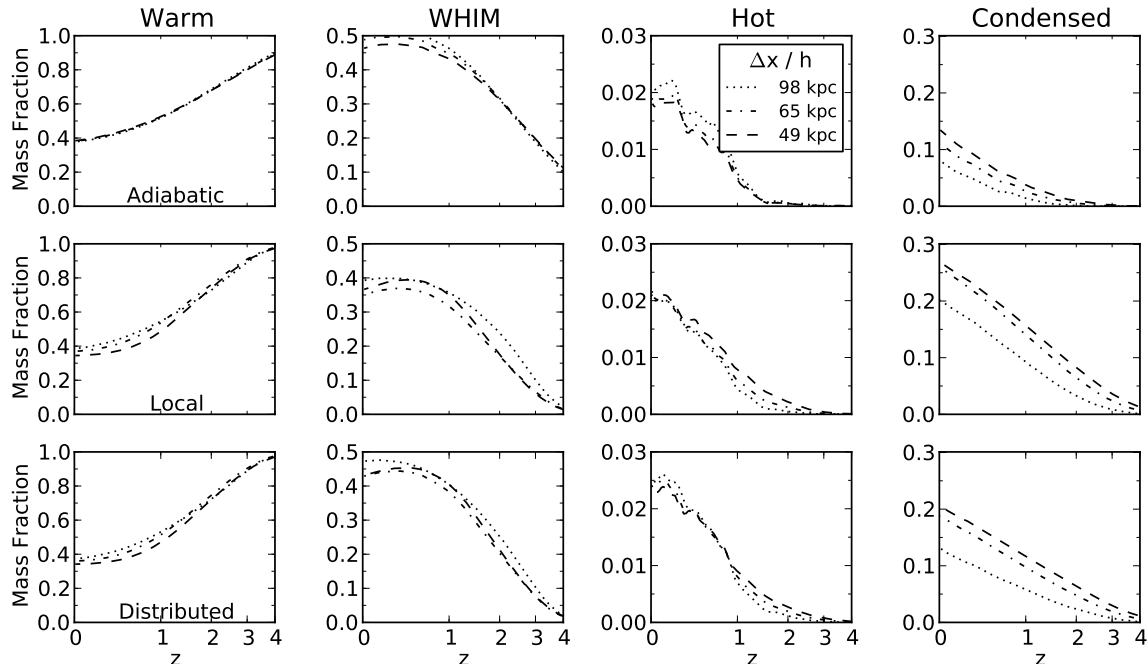


Figure 5. Evolution of baryon fraction in the warm, WHIM, hot, and condensed phases for the 50 Mpc/h box simulations. The top row shows the simulations with local feedback and the bottom row shows the simulations with distributed feedback. Phase divisions are the same as in Figure 4.

decreasing to $\sim 40\%$ by $z = 0$. This is offset primarily by an increase in WHIM gas from $\sim 10\%$ to $40\text{--}50\%$ over the same interval. In the adiabatic simulations, the mass fractions of warm and hot gas evolve identically, independent of resolution. Since the box size in these simulations is rather small, massive halos with virial temperatures $T_{\text{vir}} \gtrsim 10^7$ K are practically non-existent. Thus, the fraction of hot gas remains negligible at all times. The spike in the hot gas fraction at low redshift seen in all of the simulations shown in Figure 4 occurs due to a merger. One resolution effect that exists in the adiabatic simulations is a tradeoff between decreasing WHIM gas and increasing condensed gas with increasing resolution. As the resolution increases, the increased gravitational force resolution allows more low-mass halos to collapse and cross the critical overdensity threshold to be considered condensed gas ($\rho_b/\bar{\rho}_b > 1000$) before becoming pressure supported. In addition, higher resolution allows for smaller-scale perturbations to be resolved in the initial density field, which will also increase the mass in collapsed objects.

The addition of the full complement of physical processes to the simulations significantly alters the convergence properties. For both feedback methods, an increase in resolution yields a slightly lower fraction of warm gas at $z = 0$. The trend of decreasing WHIM fraction with resolution seen in the adiabatic runs has reversed. For $z > 1$, the fraction of hot gas increases with resolution. However, by $z = 0$, the difference in hot-gas fraction is negligible. As in the adiabatic simulations, the mass in the condensed phase increases with redshift, although the precise evolution with redshift is rather different. In general, resolution effects produce relatively minor changes in the evolution of the different phases. The most severe lack of convergence exists for the warm and WHIM phases in the local feed-

back simulations. The percent differences, defined as $100 \times |x_1 - x_2| / (\frac{1}{2}(x_1 + x_2))$, in the warm and WHIM phases at $z = 0$ between the highest and second-highest resolution simulations with 25 Mpc/h box size and local feedback are 12% and 17%, respectively. For the corresponding distributed-feedback simulations, the percent differences for the warm and WHIM phases are 9.5% and 4.4%. Thus, it is difficult to argue that the 25 Mpc/h simulations are completely converged.

The larger box simulations (Figure 5) show a greater degree of convergence. The percent differences for the 50 Mpc/h simulations analogous to those given above are 6.9% (warm) and 4.0% (WHIM) with local feedback and 5.0% (warm) and 0.2% (WHIM) with distributed feedback. Since the star formation rate is the aspect of these simulations that is furthest from convergence, this may suggest that creation of WHIM gas via gravitational shock heating dominates over stellar feedback for larger box sizes. Unfortunately, due to computational cost, we were unable to investigate this by running any simulations with $l \geq 50$ Mpc/h at the same resolution as our most refined 25 Mpc/h simulation. However, as we continue to optimize our numerical methods and the available computational resources increase, we will perform additional simulations with larger box sizes and higher dynamic range.

3.3.2. Redshift Evolution and Feedback

All of our simulations display a behavior, seemingly unique to this work, with respect to the evolution of the WHIM gas fraction. The amount of WHIM peaks at $z \approx 0.5$ and is in decline when the simulation reaches the current era ($z = 0$). This coincides with the fraction of warm gas levelling out, as opposed to continuing to decrease. Although there is no reason to believe that $z = 0$ is a “privileged epoch,” our result is in contrast to most

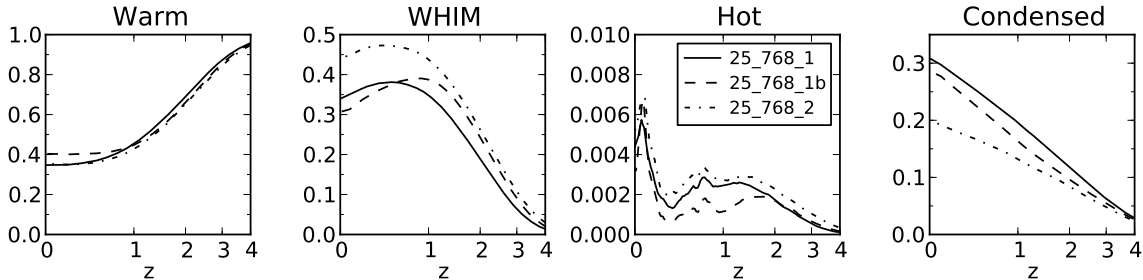


Figure 6. Evolution of baryon fraction in each phase for the three runs with 25 Mpc/h box size and 768^3 grid cells. Shown are two simulations with local feedback, one with metal yield, $y = 0.025$ (solid), and one with $y = 0.005$ (dashed), and one simulation with distributed feedback and $y = 0.025$ (dot-dashed).

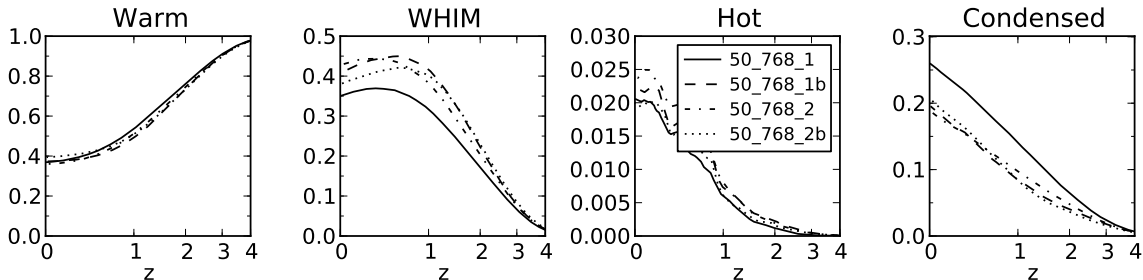


Figure 7. Evolution of baryon fraction in each phase for the four runs with 50 Mpc/h box size and 768^3 grid cells. Shown are two simulations with local feedback, one with $y = 0.025$ (solid) and one with metal yield $y = 0.005$ (dashed), plus two simulations with distributed feedback, one with $y = 0.025$ (dot-dashed) and one with $y = 0.005$ (dot).

other numerical studies, which find the WHIM fraction to still be climbing at $z = 0$ (Cen & Ostriker 1999, 2006; Davé et al. 2001; Shen et al. 2010). The recent simulations of Cen & Chisari (2010) show the evolution of the WHIM fraction to flatten out at low redshift rather than continuing to increase. The “constant-wind” model of Davé et al. (2010) shows a decline in WHIM fraction at late time, although it is the only one of their simulations to display this behavior. The “BH” model of Tornatore et al. (2010) also shows a decreasing WHIM fraction at low redshift. However, that simulation, which was also the only one in that work to feature this result, was designed specifically to have feedback from super massive black holes, which we do not include. Hence, it is somewhat unclear why our results agree. Although the adiabatic simulations show this behavior as well, it is more pronounced in the simulations with cooling and feedback.

In order to better understand this phenomenon, we attempt to measure the “flux” of gas from one phase to another in a rather crude manner. We consider flux between phase A to phase B to exist when a single grid cell changes from phase A to phase B when measured in two temporally nearby data outputs of a simulation. The value of the flux from one phase to another is simply taken to be the mass in the later data output of the cell that has changed phase divided by the time interval between data outputs. Unfortunately, we are unable to account for the change in amount of baryons in a given phase resulting from a change in density in cells that do not move from one phase to another. While this method is clearly flawed, to the extent that the exact numerical values should not be trusted, it does add useful qualitative insight.

To disentangle the contributions of cooling and feed-

back from cosmological evolution, we first perform this analysis on run 50_1024.0, the largest of our adiabatic simulations. For this exercise only, we divide the WHIM phase into two phases, the warm-WHIM ($10^5 \text{ K} \leq T \leq 10^6 \text{ K}$) and the hot-WHIM ($10^6 \text{ K} \leq T \leq 10^7 \text{ K}$). As the fraction of gas in the warm phase decreases ($z \gtrsim 1$), we measure a net flux *from* the warm phase *to* the warm-WHIM phase. At the same time, we also see a net flux *from* the warm-WHIM *to* the hot-WHIM. At low redshift ($z \lesssim 1$), where the evolution of the warm fraction appears to flatten out, the flux reverses with warm-WHIM gas now moving back into the warm phase. Likewise, hot-WHIM gas now begins flowing back into the warm-WHIM phase. In simulations without radiative cooling, the only means of cooling is adiabatic expansion. This seems to suggest that, irrespective of cooling and feedback, the universe undergoes an epoch of heating fueled by shocks from structure formation followed by an epoch of cooling due simply to the acceleration of the Hubble flow. For the cosmological parameters used in this work, the expansion factor ($E(z) \equiv [\Omega_m(1+z)^3 + \Omega_\Lambda]^{1/2}$) is dominated by Ω_Λ for $z \lesssim 0.4$, which is consistent with the epoch at which the WHIM fraction begins to decrease in our simulations. When analyzing run 50_1024.2 in the same manner, we find a similar picture. In Figure 8, we plot the net phase flux for the warm, warm-WHIM, hot-WHIM, and hot phases for run 50_1024.2. From this figure, the epochs of heating and cooling are quite visible, with the reversal of net input to net output occurring earlier in the higher temperature phases. In Figure 9, we plot the contribution of each phase to the input and output of the warm and warm-WHIM phases. It is clear from Figure 9 that the warm-WHIM is supplied with material from cooler phases at early times during the epoch

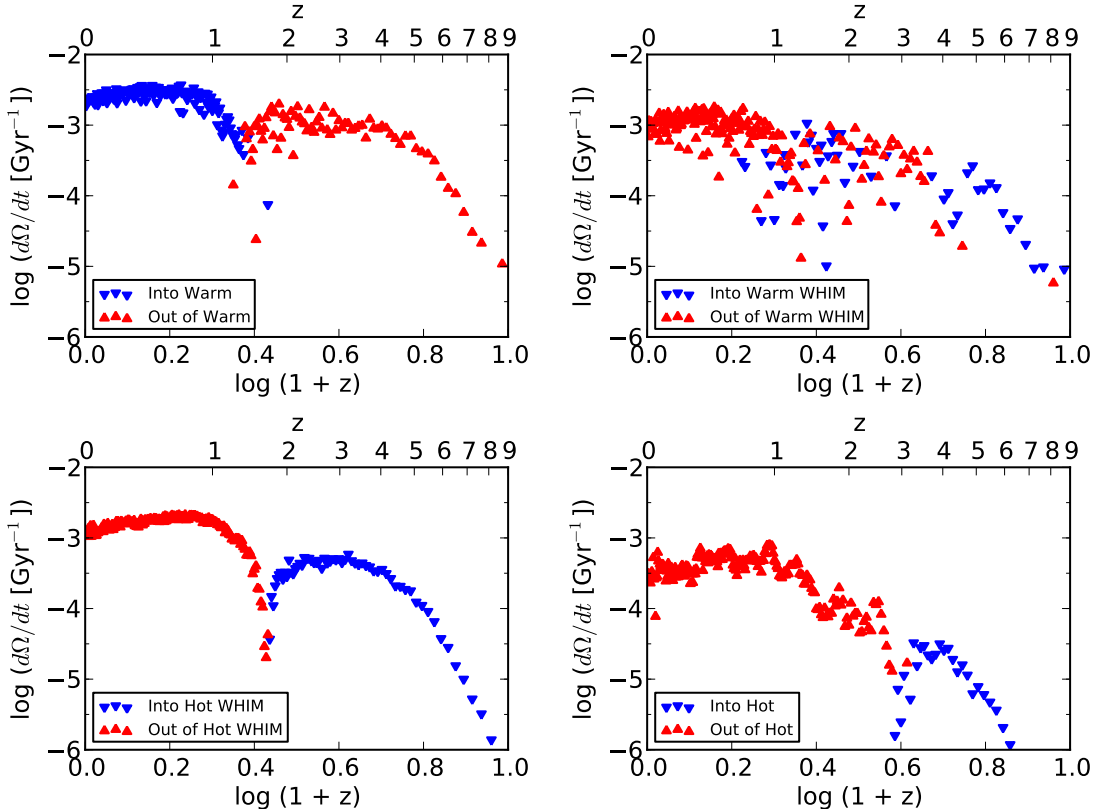


Figure 8. The net flux of baryons into and out of each phase in run 50_1024.2. Top-left: warm ($T < 10^5$ K), top-right: warm-WHIM ($10^5 \text{ K} \leq T < 10^6$ K), bottom-left: hot-WHIM ($10^6 \text{ K} \leq T < 10^7$ K), bottom-right: hot ($T \geq 10^7$ K).

of heating, and from hotter phases at late times during the epoch of cooling. Likewise, material leaves the warm-WHIM phase moving mostly into hotter phases earlier on, and then cooler phases later.

The overall contribution of radiative cooling and feedback to the evolution of the baryon phases is less clear, as they add both heating and cooling. With cooling and feedback included, the peak in the WHIM fraction occurs slightly earlier. In Figures 6 and 7, we focus on the influence of feedback on the evolution of the baryon phases. For both box sizes, the simulation with distributed feedback has roughly 10% more WHIM than the simulation with local feedback. The additional WHIM in the distributed feedback simulations comes at the expense of condensed gas. This is another example of the ability of the distributed method to overcome the over-cooling problem associated with local feedback. Interestingly, the runs with lower metal yield, denoted with the letter “*b*” in their labels, reach their peak WHIM fraction at systematically higher redshifts than their higher metal-yield counterparts. The WHIM fraction peaks at $z \sim 0.5$ in the higher-yield runs, but at $z \sim 0.9$ in the lower-yield runs, an offset of ~ 2.3 Gyr. At higher redshift, the low-yield runs have slightly more WHIM gas. However, the WHIM begins to decrease at earlier times, and the resulting WHIM fraction at $z = 0$ is lower. The low-yield runs also have lower condensed fractions, except in the case of run 50_768_2b. In every case, these offsets are balanced by a higher fraction of warm gas. In comparison to their high-yield analogs, the low-yield runs reach their peak

SFR slightly earlier ($z \sim 2$ as opposed to $z \sim 1.5$) and have significantly lower SFR at low redshift (roughly 0.5 dex compared to their higher-yield counterparts). Both of these can be attributed to the lower radiative cooling efficiency resulting from the decreased metal yield. These clues highlight the importance of accurate treatments of cooling and feedback in the evolution of the WHIM. The use of distributed feedback increases the WHIM fraction by transporting stellar feedback into the IGM with greater efficiency. Lowering the metal yield produces a similar effect, but it also suppresses the SFR more effectively. Interestingly, the single simulation of Tornatore et al. (2010) to show a decline in WHIM fraction at low redshift also happens to be the run in which the star formation rate is reduced by the greatest amount during that epoch. While radiative cooling may be responsible for some additional amount of gas that is just above 10^5 K, cooling into the warm phase, the majority of baryons residing in the WHIM are at low enough density that their cooling time exceeds the Hubble time. Thus, it seems that the role of radiative cooling is to enhance the ability of dense gas to cool and continue to form stars, which then inject thermal energy into the IGM, heating the gas into the WHIM phase.

3.4. O VI Absorption

Ultraviolet absorption lines of O VI (1032, 1038 Å) are believed to be excellent probes of the cooler portion of the WHIM, as the peak fraction of collisionally ionized O VI occurs at $T \sim 3 \times 10^5$ K. However, Oppenheimer &

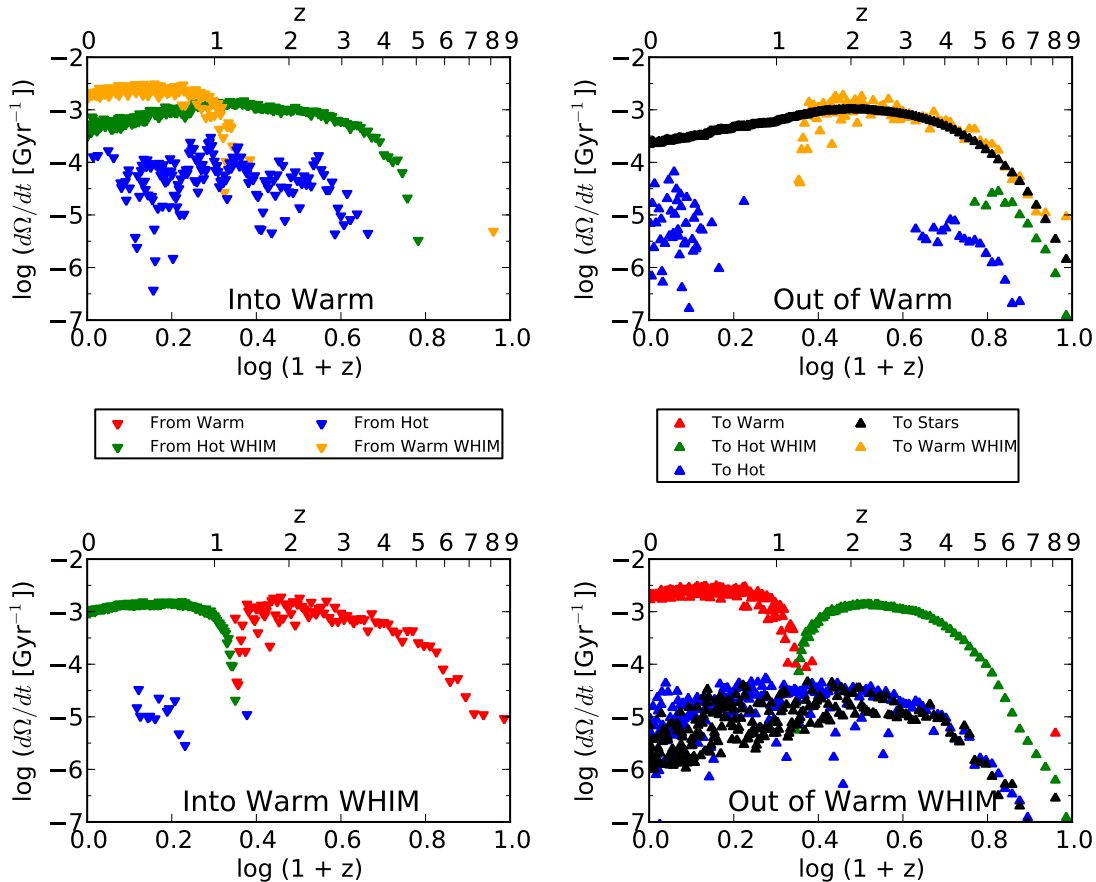


Figure 9. Inputs (left panels) and outputs (right panels) for the warm phase (top panels) and warm-WHIM phase (bottom panels) in run 50_1024_2.

Davé (2009) have claimed that the majority of O VI absorption comes from warm, photoionized gas ($T \sim 15,000$ K), although their results are likely to be affected by the significant over-cooling within their simulations. They suggest that O VI may not be a reliable WHIM tracer. Nonetheless, there exists a number of large surveys of O VI absorption lines at low redshift (Danforth & Shull 2005; Danforth et al. 2006; Danforth & Shull 2008; Tripp et al. 2008; Thom & Chen 2008a,b) that provide excellent tests of numerical simulations. In this section, we make such comparisons.

3.4.1. Creating Synthetic QSO Sight Lines

Our simulations provide a useful database that can be compared to observations of O VI and other ions along sight lines to active galactic nuclei (AGN). We use the YT⁵ (Turk 2008; Turk et al. 2011) analysis toolkit to construct a set of 500 random AGN sight lines through each of our simulations. In order to compare with the O VI absorbers in the survey of Danforth & Shull (2008), we design each sight line to extend from $z = 0$ to $z = 0.4$, the depth of the survey. Since the δz corresponding to the length of our simulation boxes is much smaller than the desired redshift depth, our sight-line generation technique involves stacking multiple rays cast through

simulation boxes from different epochs. Before running the simulations, we compute the exact number of data outputs and their location in redshift space required to traverse the comoving distance from $z = 0.4$ to $z = 0$, using ray segments no longer than the box length. For example, at $z = 0.4$, a comoving distance of 50 Mpc/ h corresponds to $\delta z \sim 0.02$. Thus, in this case, the next data output in the series is chosen to be at $z = 0.38$. We continue this process until reaching $z = 0$. For the 25 (50) Mpc/ h boxes, 47 (23) data outputs are required to span the redshift range. In this method, each sight line is able to sample the simulation box at continuously earlier epochs as it extends further away. Each individual subsegment of a given sight line has a random (x, y, z) starting position and (θ, ϕ) trajectory so as to minimize the probability of sampling the same structures more than once per sight line.

For each grid cell that is intersected by a ray, we record all relevant information of the grid cell, such as the baryon density; temperature; metallicity; redshift; path length, dl , of the ray through the cell; and the corresponding δz . Each ray length element, or lixel, is assigned a negatively incrementing redshift such that the first lixel has the same redshift as the associated data output and the last lixel has a redshift exactly δz higher than the redshift of the next data output to be used. Note that since the ray segments are randomly oriented

⁵ <http://yt.enzotools.org>

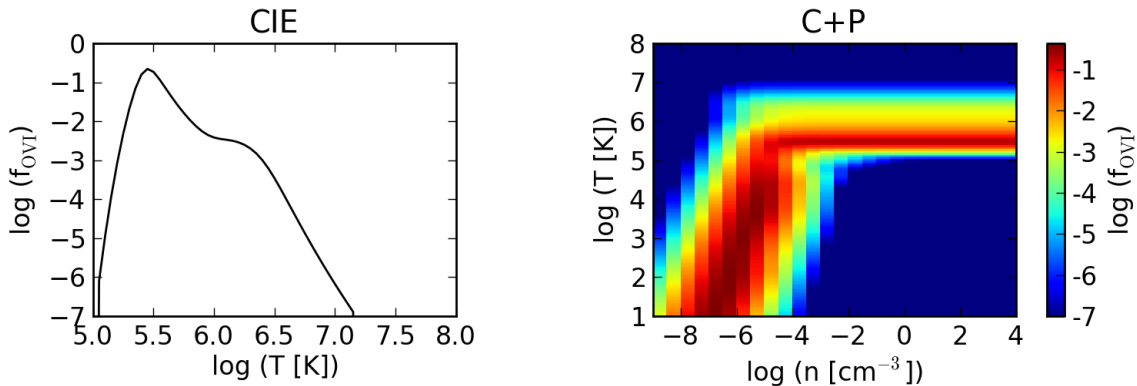


Figure 10. Left: O VI ionization fraction, f_{OVI} , in collisional ionization equilibrium (CIE) using data of Sutherland & Dopita (1993). Right: f_{OVI} calculated with `Cloudy` including collisional ionization and photoionization from a UV background at $z = 0$ (Haardt & Madau 2001).

and not necessarily parallel to any axis of the grid coordinate system, dl is not constant over an entire ray. The column density of the i 'th ionic species of a given element, X, is then given by $N_{X_i} \equiv n_{\text{H}} \times (n_{\text{X}}/n_{\text{H}}) \times f_{X_i} \times dl$, where $(n_{\text{X}}/n_{\text{H}})$ is the elemental abundance of X and f_{X_i} is the ion fraction, or (n_{X_i}/n_{X}) . A coherent structure that may produce a single absorption line in reality is almost certainly resolved over multiple pixels. In order to minimize cutting structures into multiple absorbers, we smooth each ray to a constant spectral resolution $(\lambda/\delta\lambda)$ of 5000, which is lower than the effective spectral resolution of a single grid cell. Quantities such as the temperature and metallicity of a smoothed pixel are taken as the mass-weighted averages of all contributing pixels. We do not find the resulting absorbers to be significantly affected by changes of up to an order of magnitude in either direction to the chosen spectral resolution.

Since we do not track individual heavy element species, we assume the metals are present in solar abundances patterns such that $(n_{\text{X}}/n_{\text{H}}) \equiv Z \times (n_{\text{X}}/n_{\text{H}})_{\odot}$. For the oxygen abundance, we use the value of $(n_{\text{O}}/n_{\text{H}})_{\odot} = 4.9 \times 10^{-4}$, as recommended by Asplund et al. (2005), and we employ two different methods to calculate the ionization fraction of O VI. We first consider the extreme case of no ionizing radiation, where O VI is in collisional ionization equilibrium (CIE) and f_{OVI} is only a function of temperature. For this, we use the calculations of Sutherland & Dopita (1993). We note the existence of newer calculations performed by Gnat & Sternberg (2007), based on updated ionization and dielectronic recombination rates. We intend to use these newer rates in our future work. Fortunately, the values for O VI differ only marginally between the two studies. We plot $f_{\text{OVI}}(T)$ for CIE in the left panel of Figure 10. In the second method, we assume the same UV metagalactic background (Haardt & Madau 2001) used in the simulations. We do not apply any additional renormalization to the intensity of the spectra. At $z = 0$, the mean intensity, $J_{\nu,21}$, of the background in units of $\text{m}^{-21} \text{ erg cm}^{-2} \text{ s}^{-1} \text{ Hz}^{-1}$ is 3.8×10^{-2} at 13.6 eV and 2.6×10^{-4} at 138 eV (the ionization energy of O VI). At $z = 0.4$, $J_{\nu,21}(13.6 \text{ eV}) = 0.12$ and $J_{\nu,21}(138 \text{ eV}) = 7.3 \times 10^{-4}$. When photoionization is included, the equilibrium value of f_{OVI} becomes a function of density as well as temperature. In the right panel of Figure 10, we show $f_{\text{OVI}}(\rho, T)$

calculated with `Cloudy` for the UV background at $z = 0$. For proper number densities $n_{\text{H}} \gtrsim 10^{-2} \text{ cm}^{-3}$, the equilibrium value of f_{OVI} is determined solely by electron collisions. At lower densities, photoionization begins to dominate, and the metals are typically in a higher ionization state at a given temperature than in CIE. Thus, the temperature of maximum O VI fraction decreases with decreasing density. There is significant evolution in the intensity of the UV background of Haardt & Madau (2001) between $z = 1$ and $z = 0$. We account for this when constructing the synthetic AGN sight lines by calculating f_{OVI} values for each pixel intersected by the ray segment, using interpolation tables that vary in density, temperature, and redshift. Hereafter, we will refer to this method for calculating f_{OVI} as the collisional + photoionization (C+P) model.

3.4.2. Redshift Distribution of O VI Absorbers

Numerous studies have attempted to recreate the observed number density per unit redshift of O VI absorbers as a function of column density to gauge the accuracy of their simulations (Fang & Bryan 2001; Cen & Fang 2006; Oppenheimer & Davé 2009; Tepper-García et al. 2010). In Figure 11, we plot the distribution of O VI absorbers per unit redshift per $\log N_{\text{OVI}}$ ($\partial^2 \mathcal{N} / \partial z \partial (\log N_{\text{OVI}})$) for the simulations with 25 Mpc/h box size and metal yield, $y = 0.025$. We separate runs by feedback method and plot O VI distributions calculated from both the CIE and C+P models. The number of O VI absorbers increases systematically with increasing resolution. This is not surprising, as the star formation rate, and hence the production of metals, also increases with resolution. However, it should be noted that Tepper-García et al. (2010) show the opposite trend (top-left panel of Figure B2 in Appendix B of that work), with higher resolution simulations producing fewer O VI absorbers. Just as in the evolution of the baryon phases, the simulations with distributed feedback are more converged than those with local feedback. The number of O VI absorbers at very high column density ($N_{\text{OVI}} \gtrsim 10^{15} \text{ cm}^{-2}$) is consistent at all resolutions. This is not surprising, since these absorbers are probably associated with large, collapsed structures that even the coarsest simulations are capable of resolving. The disagreement between simulations with different resolution is greater for lower column density. In all cases, the lowest resolution simulations are

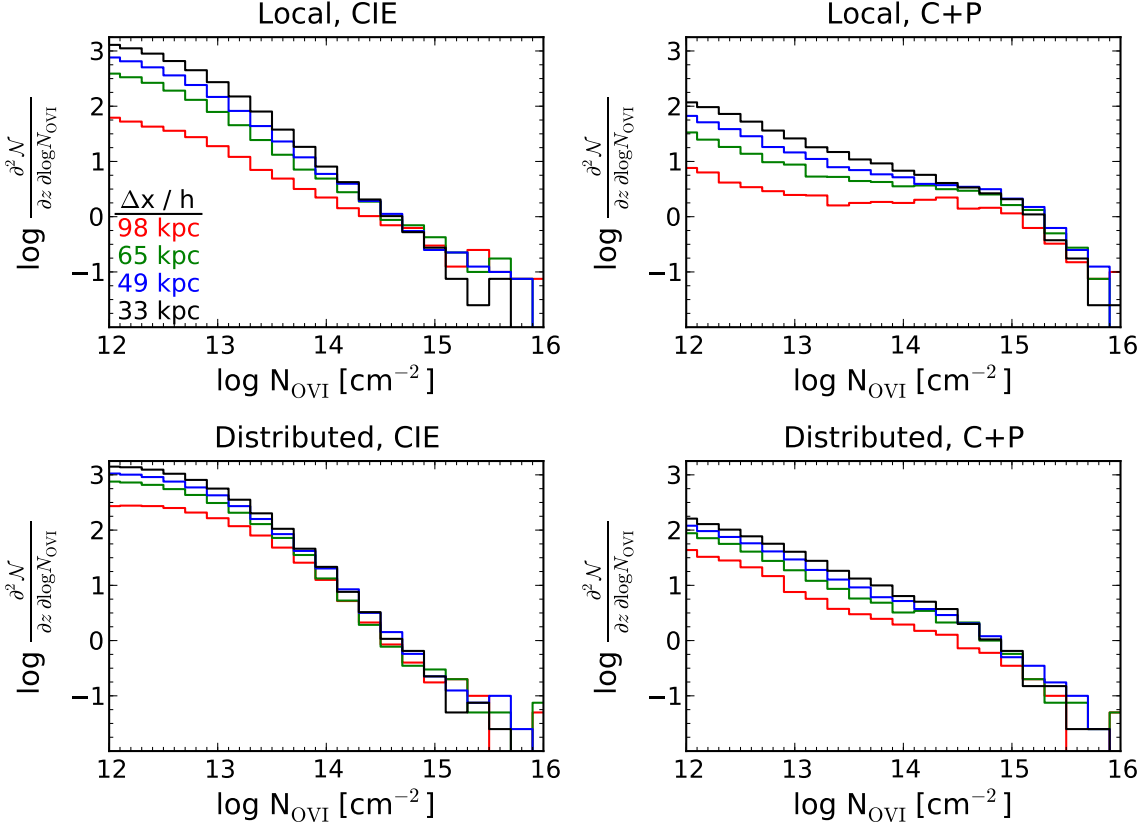


Figure 11. Convergence of $\partial^2 \mathcal{N} / \partial z \partial \log N_{\text{OVI}}$, the number density of O VI absorbers per unit redshift and per $\Delta(\log N_{\text{OVI}})$, for the simulations with 25 Mpc/h box size and metal yield, $y = 0.025$. Line colors denote the resolution of the simulations as in Figure 2. The top two panels show the simulations with local feedback, while the bottom panels show those with distributed feedback. The left panels represent O VI fractions calculated with the CIE model, while the right panels represent O VI fractions calculated with the C+P model.

grossly under-resolved with respect to the production of low column density absorbers, where we do not see full convergence. For the three highest resolution simulations, the increase in the number of O VI absorbers is roughly constant with increasing resolution. It is not completely clear what resolution is required to reach convergence. However, as we discuss below, we are able to achieve an excellent match with the observed distribution of O VI absorbers with our highest resolution distributed-feedback simulation using the C+P method, which also happens to show the greatest convergence.

In Figures 12 and 13, we plot the cumulative number of O VI absorbers, $d\mathcal{N}(>N_{\text{OVI}})/dz$, given by the integral of the bivariate distribution ($\partial^2 \mathcal{N} / \partial z \partial N_{\text{OVI}}$) over column density N_{OVI} , for our highest-resolution simulations with both 25 and 50 Mpc/h boxes. For all simulations shown, we plot the $d\mathcal{N}/dz$ resulting from f_{OVI} calculations, using both the CIE model (left panels) and the C+P model (right panels). We compare our values with the observations of Danforth & Shull (2008). The C+P model provides a much better fit to the observed $d\mathcal{N}/dz$ for $N_{\text{OVI}} \lesssim 10^{14} \text{ cm}^{-2}$. In contrast, the CIE model produces an excess of low column density O VI absorbers. As we discuss in §3.4.4, these absorbers exist primarily in regions of low baryon density and are more influenced by ionizing radiation. For higher column densities ($N_{\text{OVI}} \gtrsim 10^{14} \text{ cm}^{-2}$), the C+P model creates slightly too many absorbers. This is within the error bars for the simulations with distributed feedback, but somewhat outside for those with

local feedback. The semi-analytical models of Furlanetto et al. (2005) show steep drop-off in the number of O VI absorbers at $N_{\text{OVI}} \sim \text{few} \times 10^{14} \text{ cm}^{-2}$, which is approximately where we observe $d\mathcal{N}(>N_{\text{OVI}})/dz$ to drop below unity nearly universally. We show in §3.4.5 that the local feedback simulations have significantly more metal in regions of high overdensity, which is likely responsible for the increase in high column density absorbers. For both feedback methods, the CIE model is in closer agreement with observations for the high column density absorbers. An explanation for this is not immediately clear and may require the use of full radiation transport hydrodynamic simulations instead of the spatially uniform background employed in this work.

In general, the simulations with the standard metal yield, $y = 0.025$, display broadly similar results, independent of feedback method. The runs using the distributed method show a higher $d\mathcal{N}/dz$ for $N_{\text{OVI}} \lesssim 10^{14} \text{ cm}^{-2}$. This difference is more significant when using the CIE model. The increase in low column density absorbers from local to distributed feedback models was also seen in the simulations of Cen & Fang (2006). When photoionization is included in the f_{OVI} calculation, the runs with local feedback produce more O VI absorbers for $N_{\text{OVI}} \gtrsim 10^{14} \text{ cm}^{-2}$ than the runs with distributed feedback. With the CIE model, there is essentially no difference in the number of high column density absorbers between the two feedback methods. The $d\mathcal{N}/dz$ values for the 50 Mpc/h boxes show behavior similar to those

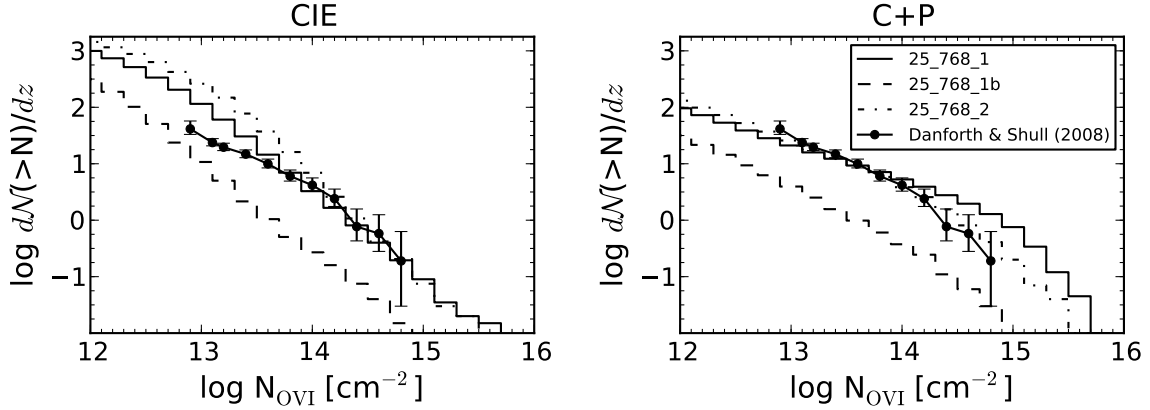


Figure 12. Cumulative number density of O VI absorbers per unit redshift as a function of column density for 500 random sight lines extending from $z = 0$ to $z = 0.4$ for runs 25_768.1, 25_768.1b, and 25_768.2, compared with the observational data of Danforth & Shull (2008). Left: f_{OVI} calculated assuming collisional ionization equilibrium (CIE). Right: f_{OVI} calculated including both collisional ionization and photoionization (C+P) from a redshift-dependent UV metagalactic background (Haardt & Madau 2001).

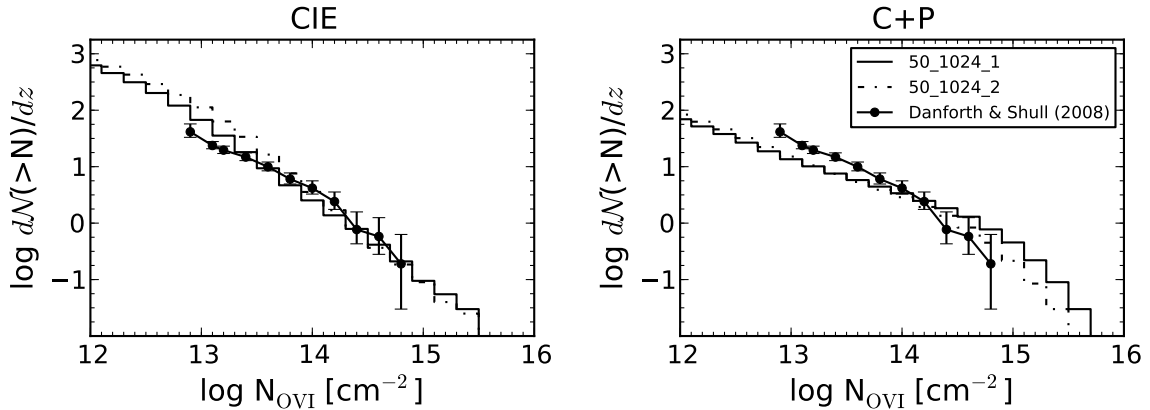


Figure 13. Same as Figure 12, except for runs 50.1024.1 and 50.1024.2.

of the 25 Mpc/ h boxes, although they are slightly lower in general. This is most likely due to the fact that the 50 Mpc/ h simulations are slightly less converged than the 25 Mpc/ h simulations. However, the dN/dz values do not appear to show any specific dependence on box size.

As expected, lowering the metal yield decreases the number of absorbers at all column densities. However, the decrease in absorber numbers is not constant over the range of column density. For $N_{\text{OVI}} > 10^{12} \text{ cm}^{-2}$, both the CIE and C+P models produce roughly 3 times fewer O VI absorbers in the low-yield run. In the CIE model, this ratio increases to a peak value of ~ 12 at $N_{\text{OVI}} \approx 10^{13.3} \text{ cm}^{-2}$, where it remains constant up to the maximum column density in the sample. For the C+P model, this ratio continues to increase over the entire range of column densities to a value of ~ 40 at N_{max} .

3.4.3. Ω_{OVI}

The ratio of the total O VI density to the closure density of the universe, or Ω_{OVI} , has been calculated for high (Carswell et al. 2002; Simcoe et al. 2004; Bergeron & Herbert-Fort 2005) and low (Tripp et al. 2000; Danforth & Shull 2008) redshift from the observed density of O VI absorption systems. Since all of these surveys have an inherent minimum column density to which they are sensitive, an important question is how much O VI goes

Table 2
 $\Omega_{\text{OVI}} (\times 10^{-7})$

Run	Simulation Box at $z = 0$		Absorption Lines $\log(N/\text{cm}^{-2}) > 12$ (13)	
	CIE	C+P	CIE	C+P
25.768.1	17	11	7.8 (4.3)	4.8 (4.5)
25.768.2	20	3.5	15 (9.4)	3.0 (2.5)
50.1024.1	7.3	3.4	5.1 (2.9)	3.0 (2.8)
50.1024.2	10	2.5	7.2 (4.5)	2.3 (2.1)

Note. — The contribution of O VI to the closure density of the universe for the four highest resolution simulations with normal metal yield. In columns 2 and 3, Ω_{OVI} is calculated by summing the total mass in O VI in the simulation box at $z = 0$ using the CIE (column 2) and C+P (column 3) models. In columns 4 and 5, Ω_{OVI} is calculated from our collection of synthetic O VI absorbers via the method described in §3.4.3.

undetected. Because the column densities of our synthetic O VI absorbers are calculated directly from the simulation data and not derived from analysis of spectra, our synthetic survey has essentially infinite sensitivity, limited only by the spatial resolution of the simulations.

We calculate Ω_{OVI} from our synthetic O VI survey by integrating over the number density of absorbers per cos-

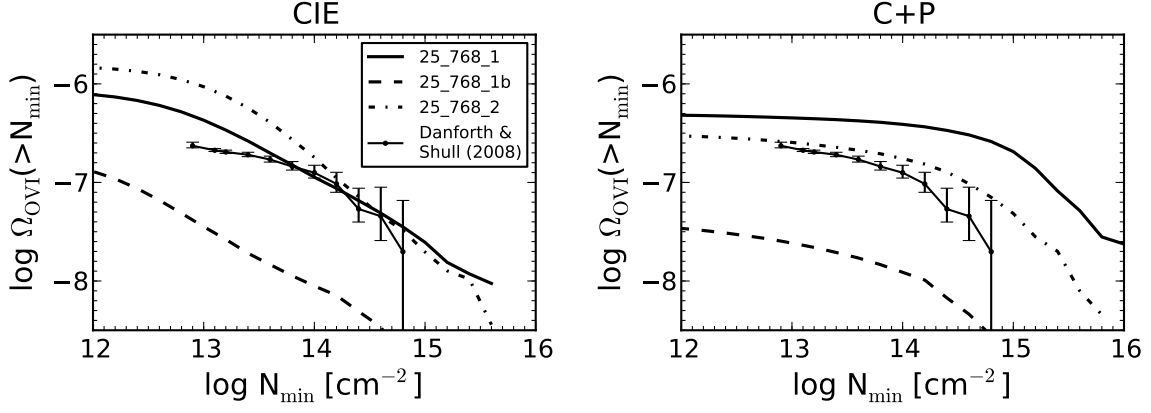


Figure 14. Ω_{OVI} as a function of minimum O VI column density for 500 random sight lines extending from $z = 0$ to $z = 0.4$ for runs 25_768_1, 25_768_1b, and 25_768_2, compared with the observational data of Danforth & Shull (2008). Left: f_{OVI} calculated assuming collisional ionization equilibrium (CIE). Right: f_{OVI} calculated including both collisional ionization and photoionization (C+P) from a redshift-dependent UV metagalactic background (Haardt & Madau 2001).

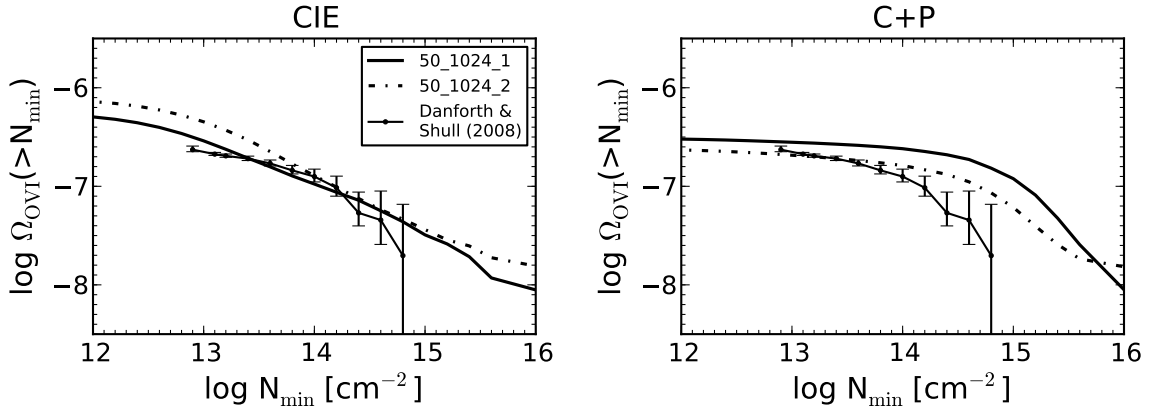


Figure 15. Same as Figure 14, except for runs 50_1024.1 and 50_1024.2.

mological path length. This is expressed as

$$\Omega_{\text{OVI}} = \frac{H_0 m_{\text{OVI}}}{c \rho_{cr,0}} \int_0^{X_{max}} \int_{N_{min}}^{N_{max}} \frac{\partial^2 \mathcal{N}(N)}{\partial X \partial \log N} N d \log N dX, \quad (4)$$

where H_0 is the Hubble constant in units of s^{-1} , m_{OVI} is the O VI mass, c is the speed of light, $\rho_{cr,0}$ is the critical density of the universe at $z = 0$, and dX is the ‘‘absorption path length function’’, defined by Bahcall & Peebles (1969) as

$$dX \equiv (1+z)^2 [\Omega_m(1+z)^3 + \Omega_\Lambda]^{-1/2} dz. \quad (5)$$

The absorption path length function corrects the number density of absorbers per unit redshift for the expansion of the universe. For the redshift interval from $z = 0$ to 0.4 , $X \simeq 0.53$. Since all of our synthetic sight lines probe this redshift epoch, the total path length used in Equation 4 is simply 0.53 multiplied by the total number of sight lines. In Figures 14 and 15, we plot Ω_{OVI} as a function of the minimum O VI column density. The values of Ω_{OVI} are reflective of the values of dN/dz and, therefore, the results are very similar. The best matches to the observational data of Danforth & Shull (2008) come from the simulations with distributed feedback and using the C+P model for calculating f_{OVI} . Due to the shal-

low slope of dN/dz for low column density absorbers in the C+P model, the additional O VI mass below current sensitivity limits of $N_{\text{OVI}} \sim 10^{13} \text{ cm}^{-2}$ appears to be negligible. However, Danforth & Shull (2008) find the differential column density distribution ($\partial^2 \mathcal{N} / \partial z \partial (\log N_{\text{OVI}})$) to be proportional to $\sim N^{-2}$, implying equal mass at all column densities. Determination of the slope of the O VI distribution at low column density is a primary science goal for the newly installed Cosmic Origins Spectrograph on HST.

We have the luxury of also calculating Ω_{OVI} via direct summation of all the grid cells in the simulation box. This allows us to determine whether calculation of Ω_{OVI} in the above manner produces a biased result. In Table 2, we list the values of Ω_{OVI} calculated through direction summation using both the CIE and C+P models for each of our four highest resolution simulations. We also give the values calculated from our synthetic absorption line samples for minimum column densities of 10^{12} cm^{-2} and 10^{13} cm^{-2} . The two methods are generally in good agreement, with direct summation yielding a value roughly 10–40% higher, with the exception of run 25_768_1 in which both the CIE and C+P summed values are approximately double their counterparts.

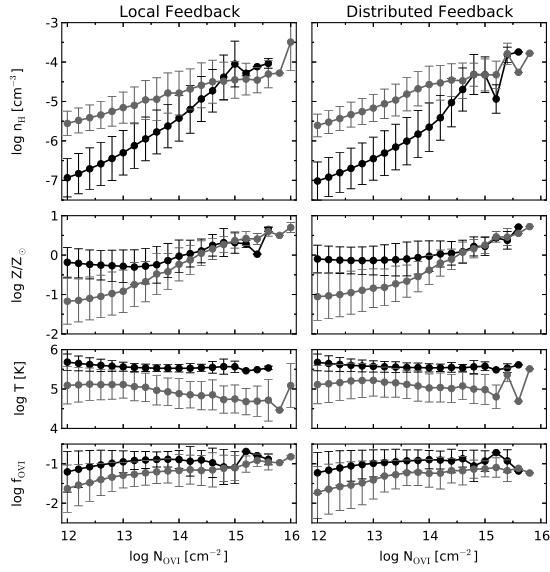


Figure 16. Mean H number density, metallicity, temperature and O VI fraction at $z = 0$, for two methods of feedback distribution. Points show 1σ deviations, with column densities of O VI absorbers shown in Figure 12 (25 Mpc/ h boxes with metal yield $y = 0.025$). Black lines show statistics for O VI fractions using CIE model and grey lines represent O VI fractions calculated with C+P model.

3.4.4. The Physical Conditions of O VI Absorbers

In Figures 16 and 17, we examine the physical conditions of the O VI absorbers plotted in Figures 12 and 13. The choice of f_{OVI} ionization model has considerable influence on the average physical conditions of the O VI absorbers as a function of their column density. For both the CIE and C+P models, the average gas density per absorber rises with column density. For the CIE model, we find $n_H \propto N_{\text{OVI}}^{0.9}$, and for the C+P model, we find $n_H \propto N_{\text{OVI}}^{0.5}$. The slope of this increase is significantly steeper with the CIE model. At the minimum column density measured, the average gas density associated with O VI absorbers from the CIE model is approximately 1.5 orders of magnitude lower than with the C+P model. For $N_{\text{OVI}} > 10^{15} \text{ cm}^{-2}$, the associated gas density is roughly similar for both models, with $n_H \approx 4.5 \times 10^{-5} \text{ cm}^{-3}$ or $\delta_H \approx 240$. With WMAP-7 parameters, $\Omega_b h^2 = 0.02260 \pm 0.00053$, the baryon density ρ_b and corresponding hydrogen number density n_H can be written

$$\begin{aligned} \rho_b &= (4.26 \times 10^{-31} \text{ g cm}^{-3})(1+z)^3 \delta_H \\ n_H &= (1.90 \times 10^{-7} \text{ cm}^{-3})(1+z)^3 \delta_H, \end{aligned} \quad (6)$$

where δ_H is the overdensity factor.

The spatial difference between O VI in the CIE model and the C+P model is made clear in Figure 18, where we show projections through the full simulation box at $z = 0$ of mass-weighted mean baryon density and temperature, along with O VI column density, using both f_{OVI} models for run 50.1024.2. With the CIE model, O VI exists spatially much further from collapsed structures, where the gas temperature is in the optimal range for O VI. However, with the C+P model, gas that would have a high f_{OVI} in CIE is instead photoionized to higher ionization states. In this case, O VI is confined primarily to IGM filaments.

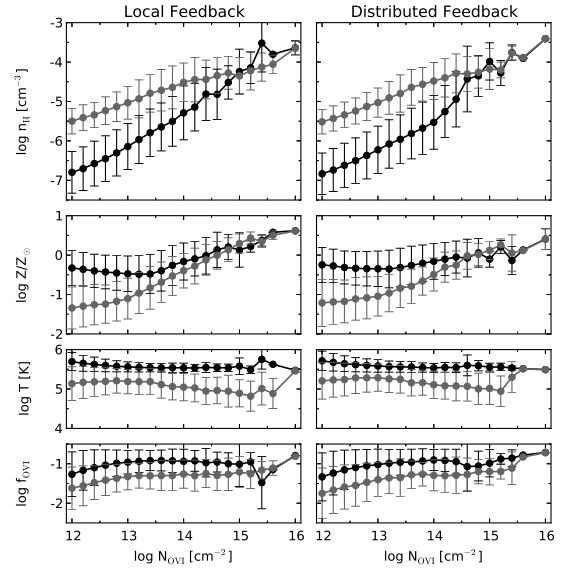


Figure 17. Same as Figure 16, but for the runs with the 50 Mpc/ h boxes shown in Figure 13.

With the CIE model, the metallicity of O VI absorbers is relatively independent of column density and consistent with $Z = Z_\odot$ up to $N_{\text{OVI}} \approx 10^{15} \text{ cm}^{-2}$. With the C+P model the metallicity rises with column density from $\sim 10^{-1} Z_\odot$ at $N_{\text{OVI}} = 10^{12} \text{ cm}^{-2}$ to Z_\odot at 10^{15} cm^{-2} . The C+P model results are similar to the findings of Cen & Fang (2006), who see a rise from just over $0.1 Z_\odot$ to slightly under Z_\odot . The density and metallicity values from the C+P models are broadly consistent with the results of Oppenheimer & Davé (2009), who employ a similar method for calculating f_{OVI} . The average absorber temperature remains fairly constant as a function of column for both f_{OVI} models. For the CIE model, the average temperature is $\sim 3 \times 10^5 \text{ K}$, with a small variance. This is not surprising, as the peak value of f_{OVI} in CIE is sharply peaked around this temperature. For the C+P model, the average absorber temperature is $\sim 10^5 \text{ K}$. Unlike the density and metallicity values, this is in considerably less agreement with Oppenheimer & Davé (2009), who find the mean absorber temperature to be $\sim 15,000 \text{ K}$. This is most likely due to the higher cooling rates in that work resulting from not accounting for the radiation background when computing the cooling with metals. The mean value of f_{OVI} is roughly 0.1 with the CIE model over the entire range of column densities. The values of f_{OVI} from the C+P model are typically lower than the CIE values by ~ 0.5 dex for $N_{\text{OVI}} \lesssim 10^{15} \text{ cm}^{-2}$. The highest column density absorbers ($N_{\text{OVI}} \gtrsim 10^{15.5} \text{ cm}^{-2}$) tend to exist as a result of particularly optimal conditions for O VI: high gas densities in excess of 10^{-4} cm^{-3} , super-solar metallicities, and values of f_{OVI} near the maximum allowable in either CIE or C+P models.

For the highest resolution 25 Mpc/ h simulations with normal metal yield, the run with local feedback forms approximately 66% more stars, and has essentially the same proportion of metals, compared to the run with distributed feedback, yet it produces 38% fewer O VI absorbers with $N_{\text{OVI}} \geq 10^{12} \text{ cm}^{-2}$. How is this possible? To answer this question, we examine the distri-

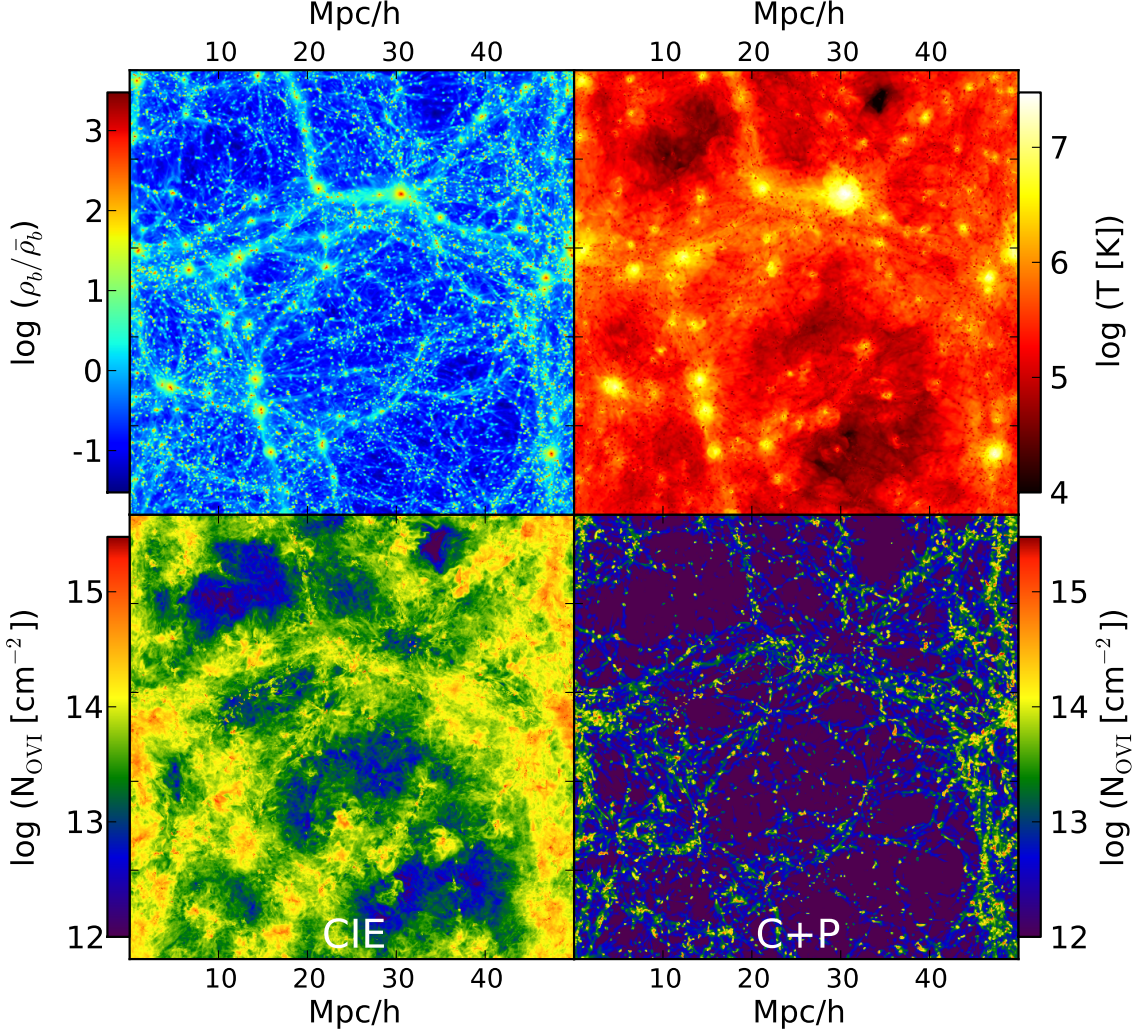


Figure 18. Projections through the full simulation box of run 50_1024_2 at $z = 0$ of mass-weighted mean baryon overdensity (top-left), mass-weighted mean temperature (top-right), and O VI number density, with f_{OVI} calculated assuming CIE (bottom-left) and including photoionization (C+P, bottom-right). Projections are constructed by summing the values in all grid cells along the line of sight. For weighted projections, each pixel in the image is calculated as $\sum_i m_i w_i / \sum_i w_i$, where m_i is the projected quantity and w_i is the weighting quantity. For more information, see Turk et al. (2011).

bution of gas-phase baryon (Figure 19) and metal mass (Figure 20) in bins of baryon overdensity and temperature for runs 25_768_1 and 25_768_2. In runs 25_768_1 and 25_768_2, $\sim 75\%$ and 85% of the total baryon mass is in the gas-phase, as opposed to in stars. The distribution of baryons in the two simulations is qualitatively similar, but there are subtle differences. The simulation with local feedback has a significant population of warm, high density baryons ($T \lesssim 10^5$ K, $\rho_b/\bar{\rho}_b \gtrsim 10^4$), not present in the simulation with distributed feedback. Instead, the distributed-feedback simulation shows an increased amount of hotter, slightly less dense baryons ($T \sim 10^7$ K, $\rho_b/\bar{\rho}_b \sim 10^{2-3}$), and more baryons in lower density WHIM as well. Recall from Figure 6 that the local feedback run has a WHIM mass fraction of 34% at $z = 0$, compared to 44% in the distributed-feedback run.

When considering the distribution of metals, the two simulations appear even more distinct. A significant portion of the gas-phase metals in the local feedback run exist in the warm, high-density gas that is not present in the

distributed-feedback run. These metals are newly created by stars, yet unable to escape their points of origin due to over-cooling. While the two runs produce roughly the same number of gas-phase metals, the run with local feedback produces significantly more metals in stars. Defining $\Omega_{\text{metals},*}$ and $\Omega_{\text{metals},\text{gas}}$ to be the total amount of metals in stars and gas with respect to closure density of the universe, we find $\Omega_{\text{metals},*} = 1.17 \times 10^{-3}$ and $\Omega_{\text{metals},\text{gas}} = 3.93 \times 10^{-4}$ for the run with local feedback and $\Omega_{\text{metals},*} = 4.81 \times 10^{-4}$ and $\Omega_{\text{metals},\text{gas}} = 3.89 \times 10^{-4}$ for the run with distributed feedback. In contrast, the distributed-feedback simulation shows far more metals in the WHIM phase. To be exact, of the metals not in stars, 44% by mass are in the WHIM phase in the local simulation, whereas 73% are located in the WHIM in the distributed simulation. Differencing the two panels of Figure 20 reveals that the greatest increase in metal mass, from the local to the distributed simulations, lies on an adiabat extending from $T \sim 10^7$ K and $\rho_b/\bar{\rho}_b \sim 10^3$ directly into the heart of the WHIM. These are metals

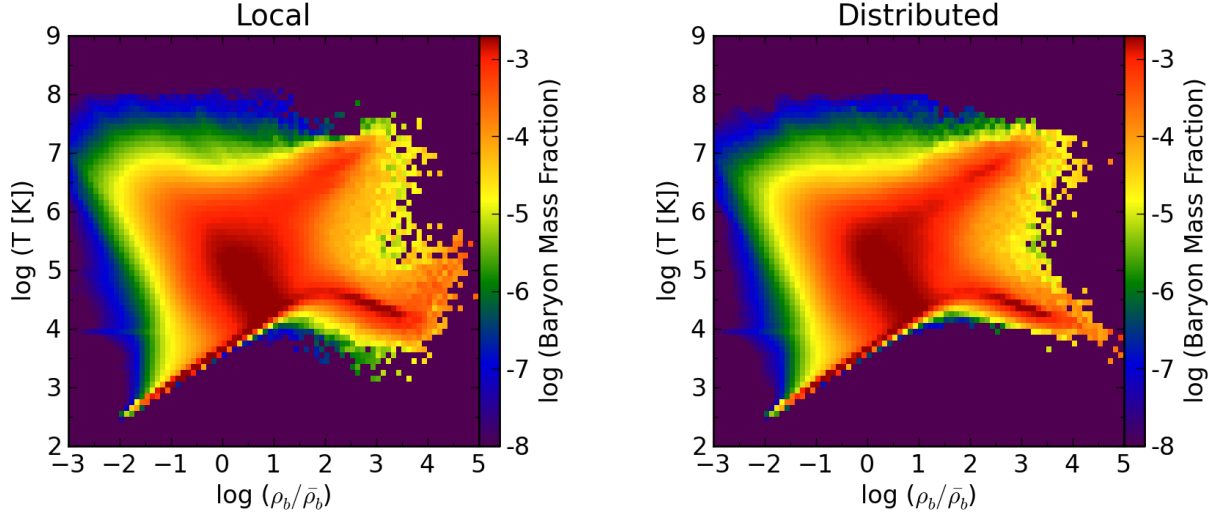


Figure 19. Fraction of total gas-phase baryon mass in two-dimensional bins of overdensity ($\rho_b/\bar{\rho}_b$) and temperature for runs 25.768.1 (left) and 25.768.2 (right) at $z = 0$. The concentration of baryons in the thin red line extending from $\rho_b/\bar{\rho}_b \sim 10^{-2}$ and $T \sim 300$ K up to $\rho_b/\bar{\rho}_b \sim 10^2$ and $T \sim 10^{4.5}$ K represents unenriched (see Figure 20 for an indication of metallicity) IGM lying on an adiabat. Radiative cooling becomes important at higher densities, as evidenced by the declining baryon temperature. The baryon concentration in the regime of $10^2 \lesssim \rho_b/\bar{\rho}_b \lesssim 10^4$ and $10^4 \text{ K} \lesssim T \lesssim 10^5 \text{ K}$ depicts collapsing halos, galaxies, and star-forming regions. Virialization shocks and stellar feedback heat gas up to $\sim 10^7$ K where it travels out into the IGM, cooling adiabatically. The adiabat extending from $\rho_b/\bar{\rho}_b \sim 10^3$ and $T \sim 10^7$ down into the broad plume of baryons between 10^5 K and 10^7 K is the WHIM. The fraction of total baryon mass in gas (not stars) is 75% for run 25.768.1 and 85% for run 25.768.2.

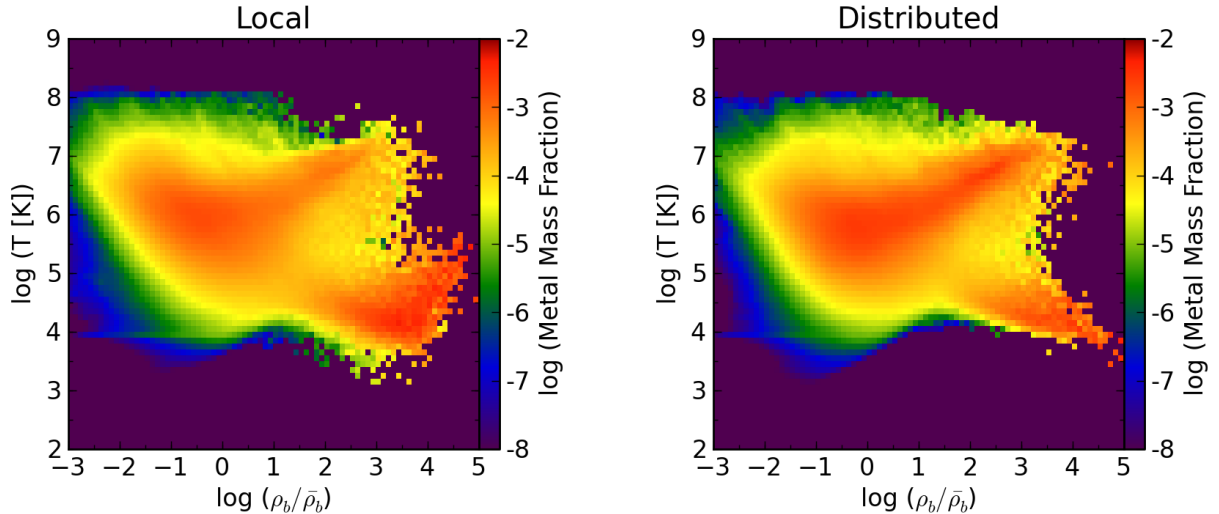


Figure 20. Fraction of total gas-phase metal mass in two-dimensional bins of overdensity ($\rho_b/\bar{\rho}_b$) and temperature for runs 25.768.1 (left) and 25.768.2 (right) at $z = 0$. The primary regimes of metal population are the galaxies and the WHIM. Although the total amount of gas-phase metals produced is roughly equivalent between the two runs, the amount of metals in stars is much higher for run 25.768.1. The fraction of the total metal mass in gas (not stars) is 25% for run 25.768.1 and 45% for run 25.768.2.

outflowing from galaxies into the IGM, cooling adiabatically as they expand into underdense gas. In summary, even though the local feedback simulation produces more metals, most of them become locked up in their host galaxies, unable to escape into the IGM. In contrast, the distributed-feedback simulation creates overall fewer metals, but it transports them into the WHIM far more efficiently.

3.4.5. Does O VI Trace the WHIM?

In order to answer this question, we plot the distribution of O VI mass from the C+P model in bins of temperature and baryon overdensity for run 50.1024.2

at $z = 0$ in the left panel of Figure 21. From this, we can see that the impression given by Figure 16 that the mean temperature of O VI absorbers is $\sim 10^5$ K is misleading. Instead, it appears that O VI has a bimodal distribution in temperature, with populations existing at $\sim 10^{4.5}$ K (mostly photoionized) and at $\sim 10^{5.5}$ K (primarily collisionally ionized). We do not see any significant fraction of O VI at $T \sim 15,000$ K, as claimed by Oppenheimer & Davé (2009). For the simulation shown, the fractions of total O VI mass are: 55% in the WHIM, 37% in the warm phase, and 8% in the condensed phase. The fraction of O VI in the hot phase ($T > 10^7$ K) is negligible.

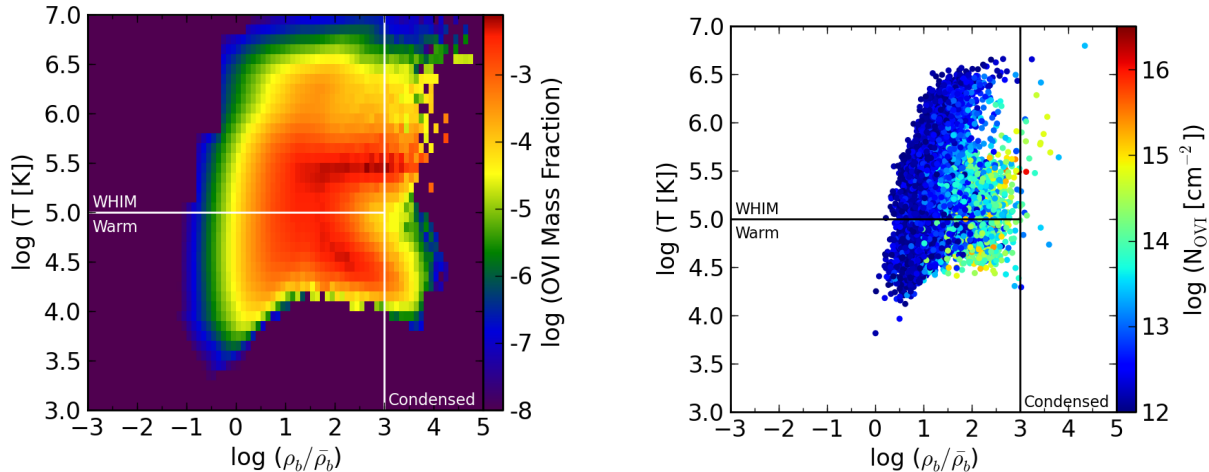


Figure 21. Left: fraction of total O VI mass in two-dimensional bins of baryon overdensity ($\rho_b/\bar{\rho}_b$) and temperature for run 50_1024.2 at $z = 0$. Right: baryon overdensity and temperature associated with each synthetic O VI absorber in run 50_1024.2 (right panel of Figure 13). Colors correspond to the column density of the absorber. In each panel, solid lines delineate divisions between the warm, WHIM, and condensed phases, as described in §3.3.

Given these statistics, the next question is: *Are these phases proportionally represented by the O VI absorbers?* In the right panel of Figure 21, we plot each one of the synthetic O VI absorbers created for run 50_1024.2, using the C+P model, on the plane of baryon overdensity and temperature with which they are associated, coloring each absorber according to column density. With respect to the total column density, 59% of the synthetically observed O VI is in the WHIM, with 36% in the warm phase and 5% in the condensed phase. Given the somewhat arbitrary definition of the condensed phase, the calculated fraction of O VI in this phase is not likely to be a very robust quantity. If we consider only O VI absorbers with column densities greater than 10^{13} cm^{-2} , closer to the observable range of O VI with HST and FUSE, the fraction in the WHIM decreases to 57%, the warm fraction increases to 37%, and the condensed fraction increases to 6%. This indicates that there is little biasing of the observed O VI away from the true O VI distribution. In contrast, the simulations of Tepper-Garcia et al. (2010) show a similar distribution of O VI mass (bottom panel of Figure 3 in that work), yet do not produce a significant number of O VI absorbers in the warm phase.

4. DISCUSSION AND SUMMARY

We have performed a series of cosmological simulations designed to study the evolution of the WHIM and its observability in low-redshift O VI absorption lines. The primary goals of this work are to find an optimal parameterization of the processes of star formation and feedback and to understand the extent to which the results of these simulations are converged and can be trusted. We investigated two methods of depositing stellar feedback onto the simulation grid: (1) injecting all of the gas, metal, and thermal energy created by a star particle into the single cell in which it is located (local feedback); (2) distributing this feedback evenly over the central cell and its 26 nearest neighbors (distributed feedback). At low redshift ($z \lesssim 1$), the local-feedback simulations show star formation rates (SFRs) much higher than observed. This appears to be the result of over-cooling that occurs when the injection of thermal energy into a single grid

cell results in an unphysically high cooling rate. We find that using the distributed-feedback method significantly lowers the low-redshift SFR and provides a much better fit to observations. For both feedback models, the SFR appears converged with respect to spatial and mass resolution at low redshift. At high redshift, the simulations are far from converged, even though the SFRs of the highest-resolution runs are not in significant disagreement with observations, however unreliable these observations may currently be. Nevertheless, the final mass in stars is reasonably well converged, as the bulk of cosmic time occurs at low redshift.

The choice of feedback method has a significant impact on the fraction of baryons in the WHIM. For our highest-resolution simulations, there is a 10% difference in WHIM fraction at $z = 0$, with $\sim 35\%$ of baryons in the WHIM in the local-feedback simulation and $\sim 45\%$ in the distributed-feedback simulation. However, these results are not totally converged. There is a significant lack of convergence in the WHIM fraction for the 25 Mpc/ h box simulations with local feedback. The distributed-feedback simulations appear much closer to convergence on the WHIM fraction. However, those runs still show a slight increase in condensed gas and a decrease in distributed gas with increasing resolution. It is encouraging that the baryon fractions for the distributed-feedback simulations of both box sizes are in good agreement with each other. In slight contrast to other work on this subject, e.g., Cen & Ostriker (2006); Davé et al. (2001), we do not see the fraction of WHIM gas continuing to rise at $z = 0$. Instead, all our simulations show the WHIM fraction to peak at $z \sim 0.5$, then decrease by a few percent by the present day. As noted above in §3.3.2, a small number of simulations in other works have shown a decline in WHIM fraction at late time. However, none of those studies see this phenomenon to be as ubiquitous as we do. We find that the decline in WHIM is offset by a leveling off of the warm gas fraction that is decreasing until $z \sim 0.5$ and a continual increase in the condensed fraction. By measuring the flux of baryons from one phase to another, we see that the universe undergoes an epoch of heating fueled by the formation of

structure, followed by an epoch of adiabatic cooling when the Hubble flow begins to accelerate due to the influence of Ω_Λ . Encouragingly, the redshift at which Ω_Λ becomes dominant ($z \sim 0.4$, with the cosmological parameters used here) is consistent with when we observe the WHIM fraction starting to decrease. Radiative cooling has two effects. The total amount of condensed gas is increased by the addition of radiative cooling, coming at the expense of WHIM gas. However, radiative cooling, primarily from metals, also enables dense gas to recool after being heated by stellar feedback, allowing it to continue to form stars and inject heat into the IGM.

We used our highest-resolution simulations to create populations of synthetic O VI absorbers. We compared these with the observed number density per unit redshift (dN/dz) of O VI absorbers from $z = 0$ to $z = 0.4$ as measured by Danforth & Shull (2008). We experimented with two methods for calculating the fraction of oxygen in O VI: the CIE model, which assumes collisional ionization equilibrium, and the C+P model, which adds photoionization from the UV background of Haardt & Madau (2001). Overall, the distributed-feedback simulations, in conjunction with the C+P model for computing f_{OVI} , provide the best match to the observations. The C+P model provides an exceptional fit for low column density absorbers with $N_{\text{OVI}} \lesssim 10^{14} \text{ cm}^{-2}$, but it slightly over-predicts the number of higher column density absorbers, although still within the error for the distributed-feedback simulations. The CIE model fits the dN/dz of the higher column density ($N_{\text{OVI}} \gtrsim 10^{14} \text{ cm}^{-2}$) absorbers better than the C+P model. Previous studies have also noted that low column density absorbers are better matched with photoionization models, while high column density absorbers are better matched with collisional ionization models (Cen et al. 2001; Fang & Bryan 2001; Chen et al. 2003). Furlanetto et al. (2005) used relatively simple arguments to predict the maximum column density of characteristic O VI absorbers to be slightly over 10^{14} cm^{-2} . In nearly all of our models, we observe the $dN(>N_{\text{OVI}})/dz$ of O VI to drop below unity at roughly similar column densities. Cen & Fang (2006) noted, as do we, that there is some dependence of the number of low column density absorbers on feedback method, with distributed-feedback methods producing more than local-feedback methods. This difference is much more significant when using the CIE model to calculate f_{OVI} . As is shown in Figure 18, the CIE model produces large amounts of O VI at great distances from collapsed structures, precisely where distributed-feedback methods excel over local feedback. On the other hand, the C+P model limits O VI to regions much closer to galaxies where the choice of feedback model is less likely to make such a difference. Given that the C+P model appears to be a much better fit to the observed number density of low column density absorbers, the prospects for constraining the properties of galactic outflows with O VI may be limited. In ionization equilibrium with the C+P model, collisional ionization is dominant for $n \gtrsim 10^{-2} \text{ cm}^{-3}$ (Figure 10). However, the mean baryon density associated with O VI absorbers with the high column density O VI absorbers is between $\sim 4 \times 10^{-6} \text{ cm}^{-3}$ and $\sim 4 \times 10^{-4} \text{ cm}^{-3}$, or overdensities ranging from $\delta_H \approx 23$ –2,300 at $z = 0$. Future simulations that incorporate radiation transport will likely be

required to fully understand why the influence of photoionization appears to be reduced in these regions.

The average physical conditions sampled by the two O VI ionization models are quite different, especially for low column densities. The highest column density absorbers, with $N_{\text{OVI}} \sim 10^{15} \text{ cm}^{-2}$, have similar properties in both models and typically result from the rare combination of high physical density, high metallicity, and high f_{OVI} . In general, O VI absorbers from the CIE model have higher associated baryon densities, lower metallicities, higher temperatures, and higher f_{OVI} than those in the C+P model. In a later paper, we will investigate the implications of the covariance in these parameters for the (O VI-based) IGM baryon census. While O VI absorbers from the CIE model probe temperatures in a narrow range around the peak in f_{OVI} ($\sim 300,000 \text{ K}$), the average O VI absorber temperature in the C+P model is much closer to $100,000 \text{ K}$. This is noteworthy, as it differs significantly from the recent simulations of Oppenheimer & Davé (2009) who find O VI absorbers to have average temperatures of $\sim 15,000 \text{ K}$. Although the mean absorber temperature is $\sim 100,000 \text{ K}$ in the C+P model, a closer inspection reveals two distinct populations of O VI at $\sim 30,000 \text{ K}$ and $\sim 300,000 \text{ K}$. We find that 55% of all O VI is in the WHIM, 37% is in warm gas, and 8% is in condensed gas. These proportions, which come from summing the total O VI mass in the simulation box at $z = 0$, are reasonably well represented by the sample of synthetic O VI absorbers, with only a few percent bias toward the WHIM.

We acknowledge a number of caveats to our current work. Radiation transport and ionizing sources are not explicitly present in our simulations, nor do we include any ionizing sources or spatially varying radiation background. The radiation background is treated by altering the H/He photoionization rates in a time varying, yet spatially uniform manner. The addition of radiation transport and ionizing sources may change the results significantly, given that the O VI absorbers are observed to be clustered around filaments (Stocke et al. 2006; Wakker & Savage 2009) and thus statistically nearer to sources of ionizing radiation. We also do not track the non-equilibrium evolution of f_{OVI} , as has been done by Cen & Fang (2006) and Yoshikawa & Sasaki (2006). While Cen & Fang (2006) showed that non-equilibrium calculations of f_{OVI} can alter the dN/dz distribution in O VI column density, we were still able to fit the observations remarkably well with the C+P model. In future work, we will include a non-equilibrium calculation of the evolution of ionization fractions for oxygen and other heavy elements.

We have shown that the number of O VI absorbers depends sensitively on the metal yield from stars, but we have not included feedback processes that release metals in varying abundance patterns. For instance, Dalla Vecchia & Schaye (2008) consider the feedback from Type Ia and Type II supernovae separately. This also changes the rate of injection of thermal energy. The parameters we have chosen for our star formation and feedback methods reflect our assumption that stars form with a Salpeter IMF at all times, which is not necessarily true. Wilkins et al. (2008) have pointed out inconsistencies between the observed star formation rate and the observed stellar density; the observed SFR implies a much higher stellar

density than observed. Since we are able to match the observed evolution of SFR, our simulations are also producing too many stars. Wilkins et al. (2008) claim that this problem could be solved if the stellar IMF was more top-heavy at high redshift ($z \gtrsim 3$), an idea also supported by Tumlinson (2007). Other recent works have cited observational discrepancies that may be potentially solved with an evolving IMF with characteristic mass increasing with redshift, e.g., Davé (2008); van Dokkum (2008). Smith et al. (2009) have shown that the high-redshift CMB can suppress fragmentation in star forming clouds, leading to an IMF that evolves with cosmic time and creates additional massive stars in the past. A varying IMF would have a significant effect on the creation and dispersal of metals in the early universe, and may be sufficiently important to consider in studies of the enrichment of the IGM.

In subsequent papers, we will address the observability of the WHIM in O VII and O VIII and other important elements, such as C, N, and Ne. We will also investigate other radiation backgrounds and their influence on photoionized absorbers. The slope of dN/dz at low column density is sensitive to the shape and intensity of the radiation background, offering a means of constraining this background with simulations. In the very near future, it will be feasible to include radiation transport in these simulations. We will combine radiation transport hydrodynamics simulations with non-equilibrium treatment of ionization balance in the metal species to study the effect of local, non-uniform radiation on WHIM observables.

We are grateful to the anonymous referee for comments that considerably strengthened the paper. We thank Charles Danforth, Brian Keeney, Devin Silvia, Sam Skillman, and Matthew Turk for helpful discussions, Andrew Hopkins for kindly providing the data from Hopkins & Beacom (2006), and Stephen Wilkins for assisting us with data from Wilkins et al. (2008). This work was supported by the Astrophysics Theory Program at the University of Colorado (NASA grant NNZ07-AG77G and NSF grant AST-0707474). EJH was supported by NSF AAPF grant AST-0702923 and HST grant AR-12131. BWO was supported in part by NASA ATFP grant NNX09-AD80G. Computations described in this work were performed using the **Enzo** code developed by the Laboratory for Computational Astrophysics at the University of California in San Diego (<http://lca.ucsd.edu>) and by a community of independent developers from numerous other institutions. The YT analysis toolkit was developed primarily by Matthew Turk with contributions from many other developers, to whom we are very grateful. The simulations were performed on NICS Kraken and TACC Ranger, with computing time from Teragrid allocations TG-AST090040 and TG-AST100004.

REFERENCES

- Abel, T., Anninos, P., Zhang, Y., & Norman, M. L. 1997, *New Astronomy*, 2, 181
- Anninos, P., Zhang, Y., Abel, T., & Norman, M. L. 1997, *New Astronomy*, 2, 209
- Asplund, M., Grevesse, N., & Sauval, A. J. 2005, in *Astronomical Society of the Pacific Conference Series*, Vol. 336, *Cosmic Abundances as Records of Stellar Evolution and Nucleosynthesis*, ed. T. G. Barnes III & F. N. Bash, 25–4
- Bahcall, J. N., & Peebles, P. J. E. 1969, *ApJ*, 156, L7
- Balogh, M. L., Pearce, F. R., Bower, R. G., & Kay, S. T. 2001, *MNRAS*, 326, 1228
- Bergeron, J., & Herbert-Fort, S. 2005, *IAU Colloq.* 199: Probing Galaxies through Quasar Absorption Lines, 265
- Bookbinder, J., Cowie, L. L., Ostriker, J. P., Krolik, J. H., & Rees, M. 1980, *ApJ*, 237, 647
- Bregman, J. N. 2007, *ARA&A*, 45, 221
- Bristow, P. D. & Phillipps, S. 1994, *MNRAS*, 267, 13
- Bryan, G. & Norman, M. L. 1997, in *Workshop on Structured Adaptive Mech Refinement Grid Methods*, ed. N. Chisochoides, IMA Volumes in Mathematics No. 117 (Springer-Verlag)
- Carswell, B., Schaye, J., & Kim, T.-S. 2002, *ApJ*, 578, 43
- Cen, R. & Chisari, N. E. 2010, *astro-ph/1005.1451*
- Cen, R. & Fang, T. 2006, *ApJ*, 650, 573
- Cen, R. & Ostriker, J. P. 1992, *ApJ*, 399, L113
- . 1999, *ApJ*, 514, 1
- . 2006, *ApJ*, 650, 560
- Cen, R., Tripp, T. M., Ostriker, J. P., & Jenkins, E. B. 2001, *ApJ*, 559, L5
- Chen, X., Weinberg, D. H., Katz, N., & Davé, R. 2003, *ApJ*, 594, 42
- Dalla Vecchia, C. & Schaye, J. 2008, *MNRAS*, 387, 1431
- Danforth, C. W. & Shull, J. M. 2005, *ApJ*, 624, 555
- . 2008, *ApJ*, 679, 194
- Danforth, C. W., Shull, J. M., Rosenberg, J. L., & Stocke, J. T. 2006, *ApJ*, 640, 716
- Davé, R. 2008, *MNRAS*, 385, 147
- Davé, R., Oppenheimer, B. D., Katz, N., Kollmeier, J. A., & Weinberg, D. H. 2010, *MNRAS*, 408, 2051
- Davé, R. et al. 2001, *ApJ*, 552, 473
- Davé, R., Hernquist, L., Katz, N., & Weinberg, D. H. 1999, *ApJ*, 511, 521
- Efstathiou, G., Davis, M., White, S. D. M., & Frenk, C. S. 1985, *ApJS*, 57, 241
- Eisenstein, D. J. & Hu, W. 1999, *ApJ*, 511, 5
- Eisenstein, D. J., & Hut, P. 1998, *ApJ*, 498, 137
- Fang, T. & Bryan, G. L. 2001, *ApJ*, 561, L31
- Ferland, G. J., Korista, K. T., Verner, D. A., Ferguson, J. W., Kingdon, J. B., & Verner, E. M. 1998, *PASP*, 110, 761
- Fukugita, M., Hogan, C. J., & Peebles, P. J. E. 1998, *ApJ*, 503, 518
- Fukugita, M. & Peebles, P. J. E. 2004, *ApJ*, 616, 643
- Furlanetto, S. R., Phillips, L. A., & Kamionkowski, M. 2005, *MNRAS*, 359, 295
- Gnat, O. & Sternberg, A. 2007, *ApJS*, 168, 213
- Haardt, F. & Madau, P. 2001, in *Clusters of Galaxies and the High Redshift Universe Observed in X-rays*, ed. D. M. Neumann & J. T. V. Tran
- Hockney, R. W. & Eastwood, J. W. 1988, *Computer simulation using particles*, ed. Hockney, R. W. & Eastwood, J. W.
- Hopkins, A. M. & Beacom, J. F. 2006, *ApJ*, 651, 142
- Kang, H., Ryu, D., Cen, R., & Song, D. 2005, *ApJ*, 620, 21
- Katz, N., Weinberg, D. H., & Hernquist, L. 1996, *ApJS*, 105, 19
- Komatsu, E. et al. 2010, *astro-ph/1001.4538*
- Madau, P., Ferguson, H. C., Dickinson, M. E., Giavalisco, M., Steidel, C. C., & Fruchter, A. 1996, *MNRAS*, 283, 1388
- Olive, K. A., Steigman, G., & Walker, T. P. 2000, *Phys. Rep.*, 333, 389
- Oppenheimer, B. D. & Davé, R. 2009, *MNRAS*, 395, 1875
- O’Shea, B. W., Bryan, G., Bordner, J., Norman, M. L., Abel, T., Harkness, R., & Kritsuk, A. 2005, in *Adaptive Mesh Renement: Theory and Applications*, ed. T. Plewa, T. J. Linde, & V. G. Weirs (New York: Springer), 341
- O’Shea, B. W., Nagamine, K., Springel, V., Hernquist, L., & Norman, M. L. 2005, *ApJS*, 160, 1
- Persic, M. & Salucci, P. 1992, *MNRAS*, 258, 14P
- Schaye, J. & Dalla Vecchia, C. 2008, *MNRAS*, 383, 1210
- Schaye, J. et al. 2010, *MNRAS*, 402, 1536
- Shen, S., Wadsley, J., & Stinson, G. 2010, *MNRAS*, 1043
- Shull, J. M. 2003, in *Astrophysics and Space Science Library*, Vol. 281, *The IGM/Galaxy Connection. The Distribution of Baryons at z=0*, ed. J. L. Rosenberg & M. E. Putman
- Simcoe, R. A., Sargent, W. L. W., & Rauch, M. 2004, *ApJ*, 606, 92

- Skillman, S. W., Hallman, E. J., O'Shea, B. W., Burns, J. O., Smith, B. D., & Turk, M. J. 2010, *astro-ph/1006.3559*
- Skory, S., Turk, M. J., Norman, M. L., & Coil, A. L. 2010, *ApJS*, 191, 43
- Smith, B., Sigurdsson, S., & Abel, T. 2008, *MNRAS*, 385, 1443
- Smith, B. D., Turk, M. J., Sigurdsson, S., O'Shea, B. W., & Norman, M. L. 2009, *ApJ*, 691, 441
- Springel, V. & Hernquist, L. 2003a, *MNRAS*, 339, 289
- , 2003b, *MNRAS*, 339, 312
- Steigman, G. 2007, *Annual Review of Nuclear and Particle Science*, 57, 463
- Stocke, J. T., Penton, S. V., Danforth, C. W., Shull, J. M., Tumlinson, J., & McLin, K. M. 2006, *ApJ*, 641, 217
- Stone, J. M. & Norman, M. L. 1992, *ApJS*, 80, 753
- Sutherland, R. S. & Dopita, M. A. 1993, *ApJS*, 88, 253
- Tepper-Garcia, T., Richter, P., Schaye, J., Booth, C. M., Dalla Vecchia, C., Theuns, T., & Wiersma, R. P. C. 2010, *astro-ph/1007.2840*
- Thom, C. & Chen, H. 2008a, *ApJS*, 179, 37
- , 2008b, *ApJ*, 683, 22
- Tornatore, L., Borgani, S., Viel, M., & Springel, V. 2010, *MNRAS*, 402, 1911
- Trenti, M., Smith, B. D., Hallman, E. J., Skillman, S. W., & Shull, J. M. 2010, *ApJ*, 711, 1198
- Tripp, T. M., Savage, B. D., & Jenkins, E. B. 2000, *ApJ*, 534, L1
- Tripp, T. M., Sembach, K. R., Bowen, D. V., Savage, B. D., Jenkins, E. B., Lehner, N., & Richter, P. 2008, *ApJS*, 177, 39
- Tumlinson, J. 2007, *ApJ*, 664, L63
- Turk, M. 2008, in *Proceedings of the 7th Python in Science Conference*, ed. G. Varoquaux, T. Vaught, & J. Millman, Pasadena, CA USA, 46 – 50
- Turk, M. J., Smith, B. D., Oishi, J. S., Skory, S., Skillman, S. W., Abel, T., & Norman, M. L. 2011, *ApJS*, 192, 9
- van Dokkum, P. G. 2008, *ApJ*, 674, 29
- Wakker, B. P. & Savage, B. D. 2009, *ApJS*, 182, 378
- Warren, M. S., Abazajian, K., Holz, D. E., & Teodoro, L. 2006, *ApJ*, 646, 881
- Wiersma, R. P. C., Schaye, J., & Smith, B. D. 2009, *MNRAS*, 393, 99
- Wilkins, S. M., Trentham, N., & Hopkins, A. M. 2008, *MNRAS*, 385, 687
- Yoshikawa, K. & Sasaki, S. 2006, *PASJ*, 58, 641